Materials Advances

ROYAL SOCIETY OF CHEMISTRY

PAPER

View Article Online
View Journal | View Issue

Cite this: *Mater. Adv.*, 2025, 6, 9150

Evolution of giant exchange bias with ferromagnetic ordering and a robust memory effect by strain engineering MoS_2 in weak antiferromagnetic gating

Shatabda Bhattacharya, *[ab] Irina A. Kühne, [b] Tatsuhiko Ohto [c] and Hirokazu Tada [a]

The emergence of 2D ferromagnetism in MoS_2 layers induced by an inherently non-magnetic material like NiOOH is an interesting area of research. This result is of widespread technological importance if additionally associated with magnetic exchange correlations that show promising memory effects. In this work, we show that a giant exchange bias is housed within highly strained 2D MoS_2 multilayers by interfacing with the thin weakly antiferromagnetic β-NiOOH phase. The robustness and magnitude of such zero-field-cooled exchange bias emerge from the unique sublattice spin configuration of β-NiOOH, which serves as a source of surface uncompensated moments, while highly strained 2D MoS_2 acts as an active pinning layer in the hybrid. The exchange coupling between the weak antiferromagnetic layer and the adjacent moment-induced ferromagnetic layer is strong enough to show a near-room temperature thermoremanent (TRM) memory effect in magnetization states, which is newly observed for 2D hybrid materials. Upon manifesting the vertical type junction, this hybrid material also shows non-volatile electrical bistable states with a low operating bias voltage (1.25 V) and high ON/OFF ratio (6×10^2), along with hysteretic magnetoresistance, which can be useful in 2D-based spintronic applications. First-principles calculations also verified such charge transfer interactions at the interface of the hybrid structure.

Received 30th May 2025,
Accepted 16th September 2025

DOI: 10.1039/d5ma00565e

rsc.li/materials-advances

1. Introduction

The correlated properties of quantum hybrid materials are one of the most interesting areas of research in nanotechnology, where properties from the individual components are coupled together. In this area, transition metal dichalcogenides (TMDs) have a unique 2D van der Waals structure with the absence of dangling bonds and layer-dependent properties such as band gap tunability and mobility variation. Thus, TMDs can possibly be combined with other type of materials *via* strain engineering.[1] MoS_2, a promising TMD, has attracted enormous interest for its recent potential application in transistors, catalysis, optoelectronic devices, and other fields.[2–7] Due to its layer type structure, it can withstand large strain before breaking. Thus, strain engineering has become a hot topic of research.[8] This strategy is now wisely used to tune the property of MoS_2-based semiconducting devices. Additionally, benefiting from valley band-specific spins, the strong spin–orbit interaction in such materials is an additional parameter that can be used to control its electronic states. Despite such properties, due to the absence of inherent magnetism in MoS_2, the incorporation of magnetism into TMDs has been proposed to integrate spin–valley interaction in 2D materials. Different from direct magnetic doping, the use of the magnetic proximity effect (MPE), where an adjacent magnetic layer is employed to induce the effect, is considered an eminent strategy to gain long-range magnetic interactions in hybrid heterostructures.[9–11] In such context, ferromagnetic materials are thus far only used for this MPE effect using conducting-type metallic materials. However, for transport-related properties, magnetic conductors may short-circuit the adjacent MoS_2 layer in proximity and ultimately restrict the electrical measurement of the hybrids. In this case, other than the conducting type, antiferromagnetic insulators can be a possible substitute to this material to understand the coupling effect. Since antiferromagnets have two antiparallel spin orientations, the effect of interfacial coupling is to generate induced magnetic moment

[a] *Department of Materials Engineering Science, Graduate School of Engineering, Osaka University, Toyonaka 560-8531, Osaka, Japan*
[b] *Division of Condensed Matter Physics, FZU-Institute of Physics of the Czech Academy of Sciences, Na Slovance 1999/2, 182 00, Prague, Czech Republic. E-mail: shatabda@fzu.cz*
[c] *Graduate School of Engineering Science, Nagoya University, Furo-cho, Chikusa-ku, Nagoya, Aichi 464-8603, Japan*

in the nearby 2D template *via* the charge transfer effect. For example, in the case of graphene, when transition metals (TM) are placed in proximity to the graphene surface, an induced moment is observed in the 2D layers but the 3d orbital moment of TM is quenched due to hybridization.[12,13] Particularly, when nickel is used for inducing a moment in 2D surfaces (graphene, germanene or silicone), it is found that due to a secondary charge transfer from the metal's 4s orbital to its 3d orbital, nickel can be transformed into diamagnetic, which becomes detrimental.[14–16] Apart from these issues, the question of the formation of a metal oxide when exposing the 2D-hybrid to an open atmosphere is a long-standing problem. In TMDs, due to the sulfur-rich environment, it is more prone to interact with the nearby metal-complexes of suitable types to stabilize the structures.

Although the induction of weak ferromagnetic ordering in intrinsically non-magnetic MoS_2 by highly magnetic insulators (yttrium iron garnets: YIG) or TMs (Fe, Co, Ni) has been often observed, the role of non-magnetic metal-oxides is relatively unexplored.[17] Interest in nickel hydroxide ($Ni(OH)_2$) and its redox pair, *i.e.* NiOOH, has increased in the past few decades due to their excellent catalytic activity, battery applications, cathode material, and other properties.[18–20] The derivative of structures can be commonly called as NiOOx. The structure of NiOOx can remain in basically four phases, such as: β-$Ni(OH)_2$, α-$Ni(OH)_2$, β-NiOOH and γ-NiOOH.[21,22] The main characteristics of these four phases are that they each consist of primary NiO_2 slabs with tetrahedral coordination of H-atoms between the interslab space, which makes them interesting.[23] While α-$Ni(OH)_2$ and γ-NiOOH are poorly crystallized with turbostratic disorder, β-$Ni(OH)_2$ and β-NiOOH are relatively stable in nature.[24,25] The majority of literature studies say that the oxidation of β-$Ni(OH)_2$ to β-NiOOH leaves it in a similar hydrogen-bonded structure with the space group of $P\bar{3}m1$.[26,27] Being a more primitive and fundamentally important material, the presence of a partial Ni^{3+} state or a mixture of Ni^{2+} and Ni^{4+} in a disproportionate manner could be of interest in terms of its magnetic behaviour when attached to a 2D surface and how it can alter the magnetic state to its nearby 2D layer.[28]

In this manuscript, we report on ultrathin layers of the antiferromagnetic β-NiOOH phase (height variation ~5–20 nm), grown on a multi-layered MoS_2 surface. We have investigated the interfacial effect by tuning the number of layers. The β-phase of NiOOH is a layered structure, where the weak antiferromagnetic interactions arise at low temperatures due to superexchange coupling between the Ni^{3+} centres through oxygen. The β-phase of NiOOH with its unique partial presence of the Ni^{3+} oxidation state (in the distorted octahedra) is relatively unexplored in the area of its fundamental magnetic states, *i.e.* ground spin state condition and magnetic applications.[29] The antiferromagnetic phase induces a magnetic moment in the adjacent MoS_2 *via* the interfacial coupling effect, which results in large coercive fields (~6439 Oe) and ferromagnetic long-range interaction (~20-fold rise in the magnetization moment) with high Curie temperature in the hybrid nanostructure. The structural mismatch generates a large tensile microstrain ($\sim 10^{-2}$) in this 2D MoS_2-hybrid, which has been thoroughly characterized by X-ray Rietveld method for micro-strain analysis, transmission electron microscope (TEM) and Raman spectroscopy. Due to its high zero field cooled (ZFC) exchange bias effect (~1500 Oe) in a 2D MoS_2 based hybrid, it has been extensively tested for high-density magnetic storage devices *via* thermo-remanent magnetization procedures. It was found to exhibit exotic robustness (over long-time scales of 25 000 s) for magnetic storage applications, including voltage-mediated magnetic switching as bistable memory states. This hybrid material further showed a rewritable non-volatile electrical memory with an energy-efficient low switching bias voltage (<1.25 V) and high current ON–OFF ratio ($\sim 10^2$) compared to its conventional counter parts. The ON/OFF ratio was enhanced to 6×10^2 upon field bias using this 2D MoS_2-based hybrid material as the active layer in vertical type junctions. Such observed large ON/OFF-ratio is effective to eliminate the probability of misreading during memory testing.[30–33] The electrical bi-stability is highly voltage-dependent, resembling a reading-writing process in the vertical layered memory analogue. During the density functional theory calculation of MoS_2–βNiOOH composites, we found FM ordering for the monolayer of β-NiOOH on 2D MoS_2. Conversely, for the bilayer of β-NiOOH, which can be also considered as a thick sample, the AFM interaction was found to be in the ground state. Also at the interface, Bader charge analysis showed the finite value of the charge transfer. Hence, the 2D layer is responsible for changing the magnetic state of the adjacent NiOOH layers.

Despite the long-term study of a suitable prototypical exchange bias system, the layered AFM/2D heterostructure could give a complete understanding of the cause behind this large exchange bias effect. The pinned uncompensated surface moments in the AFM phase interacted within the interface of the highly disordered MoS_2 defect lattice *via* coupling effect. The main criteria of this type of interaction include frustration that emerges due to the site disorder or competition among local exchange interactions, resulting in interesting two-step magnetization and a sizable exchange bias (EB) effect in the 2D hybrid. The strong coupling between the AFM β-NiOOH layer and charge transfer-induced FM layer generates a high ZFC EB effect. It is found that due to this structure formation, highly field-responsive, pinned moments are embedded within the 2D matrix. They show the dependence of magnetic moment on thermal cycles, which is known as the thermoremanent magnetic memory effect, as previously studied extensively to understand the spin dynamics of hybrid 2D heterostructures.[34–36]

2. Results and discussion

A. Synthesis and structural characterizations of MoS_2/β-NiOOH hybrids

The synthesis process was carried out in two steps. In the first step, MoS_2 has been prepared under hydrothermal conditions as follows. As a source for molybdenum, we used hexaammonium heptamolybdate tetrahydrate [$(NH_4)_6Mo_7O_{24}\cdot 4H_2O$;

5 mM = 310 mg]. As a sulfur source, we used thiourea (70 mM = 268 mg) and dissolved the two compounds in 40 ml of DI water under vigorous stirring, forming a homogenous solution. This mixture was sealed in a Teflon-lined (PTFE) stainless steel autoclave, maintaining a temperature of 180 °C for 24 h. After this reaction, the black product, which is the suspended MoS_2 layers, was thoroughly washed with water and ethanol several times to eliminate unreacted molecules or excess sulfur and finally collected *via* centrifuge methods (10 000 rpm). As we have prepared two different batches of the hybrid samples, the stock solution of the parent MoS_2 was equally divided into two parts and dissolved in 50 ml anhydrous *N*,*N*-dimethylformamide (*n*-DMF) (dense solvent) and underwent ultrasonication for 2 h. During this time, the MoS_2 layers were exfoliated by the ultrasonic vibration and were well dispersed in the solution.

To this MoS_2 solution (50 ml), 50 ml nickel acetate ($Ni(OAc)_2$) aqueous solution (concentration of Ni salt, 0.1 M) was added with urea (0.002 M) and 0.1 g of polyvinyl pyrrolidone (PVP). The resulting mixture was refluxed at 50 °C for 1 h, and 1 M of NaOH solution (20 ml) was subsequently added. The final solution was autoclaved at 100 °C for 24 h. The final product was subsequently washed with water, ethanol and acetone to remove excess unreacted products of urea and PVP. They were dried under vacuum in 40 °C. According to the concentration of Ni, the sample was named as MN-1 (high concentration of NiOOH). We prepared another batch of sample with the same MoS_2, but the nickel precursor salt was (0.01 M), *i.e.* 1/10th to MN-1, and is termed as MN-2 (lower concentration of NiOOH). The concentration of the initial nickel precursor salt was directly proportional to the layer thickness of the formed nanoflakes of the NiOOH structure over MoS_2.

B. X-ray diffraction (XRD) and Rietveld refinement analysis of the composites

Powder XRD of the two nanocomposites was carried out and the profiles were obtained, as shown in Fig. 1a and b for MN-1 and MN-2, respectively. To analyse the structure pattern and strain in the composites, we fitted the experimental data using the MAUD™ program for Rietveld fitting.[37,38] The characteristic MoS_2 peaks represent hexagonal symmetry ($P6_3/mmc$) and β-NiOOH phase trigonal symmetry ($P\bar{3}m1$). The peaks were further matched with JCPDS card numbers 37-1492 (for MoS_2) and 6-0141 for the β-NiOOH phase, respectively. The red line curve corresponds to the Rietveld fitted to the experimental graph, and Table 1 shows the extracted parameters, *viz.* lattice constants, R.M.S. microstrain, crystallite size, structure equivalency, *etc.* From the overall XRD profile, it is seen that the peak intensity for the MoS_2 phase remains almost unchanged for the two samples, while the main peak of the β-NiOOH phase, *i.e.* (001), changes its intensity as the layer number is diminished from the MN-1 to MN-2 sample. There is also a large shift of the (002) plane of MoS_2 from 13.82° (MN-1) to 12.75° (MN-2) due to the interlayer tensile strain in MoS_2 along the *c*-axis ([001] direction), from which the interlayer separation has expanded (Fig. 1a). It should be noted that for MoS_2, the (002) planes may expand due to intercalation. However, in this case, it is due to the out-of-plane uniaxial tensile strain because of the heterostructure growth expanding the interlayer spacing (*c*-axis), as found in the literature by Yang *et al.*[39] Later, in the TEM analysis of the cross-sectional views of the (002) MoS_2 planes, no signature of chemical intercalation was found. Conversely, the peak of the (101) plane of MoS_2 shifts to a larger angle 2θ, *i.e.*, from 32.88° (for MN-1) to 33.03° (for MN-2), indicating in-plane biaxial compressive strain (Fig. 1c). A schematic for the MN-2 sample is shown in Fig. 1d.[39] This fact is also visualized in the TEM images and analyses given later for the strain effects in the basal planes of MoS_2. From Table 1 of the Rietveld refinement, if we carefully look at the *c*-lattice parameter of MoS_2, it changes from 12.72 Å (MN-1) to 13.76 Å (MN-2). The microstrain value calculated from the Rietveld refinement analysis for the MoS_2 phase increases from −0.008 (MN-1) to −0.059 (MN-2), which is enormously high for a strain parameter in 2D systems.[40,41] In the case of the β-NiOOH phase, there are also microstrain changes from 0.009 (MN-1) to 0.029 (MN-2). Furthermore, the '*a*'-lattice parameter decreases from 3.07 Å (MN-1) to 2.25 Å (MN-2), which is a compressive strain for the β-NiOOH phase. From this analysis, it can be concluded that for the MN-2 sample, the strain is much higher than that in MN-1 due to the thinness of the β-NiOOH layer. Furthermore, the overall MoS_2 layers are highly strained in the MN-2 sample. Fig. 1d shows a schematic diagram of the MoS_2/β-NiOOH heterostructures where for the MN-1 sample (left), the thick layer of β-NiOOH is grown on the MoS_2 surface with the interlayer separation of MoS_2 at about 6.4 Å. In MN-2, thin layers of β-NiOOH are shown with the out-of-plane tensile strain [001] direction, which expands the interlayer separation of MoS_2 to 7.6 Å and the highly strained structure is formed. Additionally, it is pertinent to mention that at the 2θ value of around 38.5° for MoS_2, the (103) plane is very weak in intensity if it comes from only the MoS_2 phase. However, as it is overlapped here with the NiOOH (100) position, it shows an increase in intensity.[42,43]

C. Transmission electron microscopy (TEM) image analysis for the growth structure

Fig. 2a shows the MN-1 sample with the overall image of the β-NiOOH layers overlapping largely on the MoS_2 surface. The right upper inset part shows the magnified β-NiOOH nanodisc. The left upper part is the selected area electron diffraction (SAED) pattern from the overall structures showing multiple diffraction spots for a large number of overlapped NiOOH layers at different angles, as observed previously.[44] Next in Fig. 2b, the basal plane of MoS_2 is shown in high-resolution (HR) mode, where the highly strained 2D layer structure can be seen in the yellow circle spotted areas with noticeable localized dark patches with the disrupted lattice continuity usually seen for highly strained 2D layer systems. The in-plane MoS_2 surface is highly strained, as evidenced from this high-resolution (HR) TEM image, which has also been found in many cases.[45,46] Next, for the MN-2 sample, comparatively thinner layers of the β-NiOOH nanodisc are shown. MoS_2 remained as a substrate

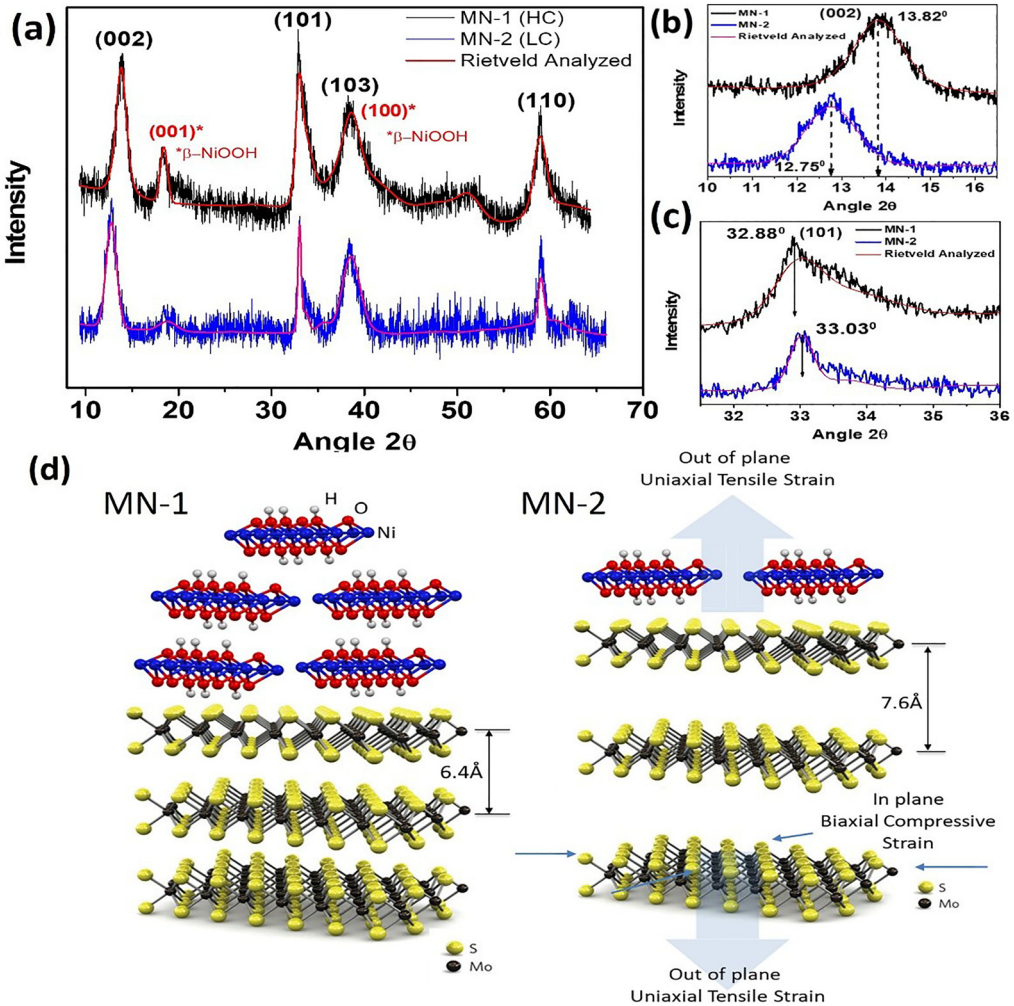

Fig. 1 (a) Powder XRD profiles of the composite samples MN-1 and MN-2, respectively, with the characteristics MOS_2 and β-NiOOH peaks. The red line is the Rietveld fitted data. (b) Magnified view of the (002) MoS_2 layer separation peaks from the previous plot. (c) Magnified view of the (100) peaks for the two composites. (d) Schematic of the two different morphologies of the β-NiOOH phase on the layered structure of MoS_2. Interlayer separation has been increased due to the out-of-plane tensile strain in the heterostructures.

Table 1 XRD parameters obtained after Rietveld refinement of the p-XRD data of the two composite samples

	Thick layer over MoS_2 (MN-1)			Thin layer over MoS_2 (MN-2)		
Phase	Lattice parameters	Value	Error (±)	Lattice parameters	Value	Error (±)
MoS_2	*a*, *b*	3.13 Å	0.002	*a*, *b*	3.12 Å	0.003
	c	12.72 Å	0.003	*c*	13.76 Å	0.004
	Microstrain	−0.008	3.2×10^{-5}	Microstrain	−0.059	4.4×10^{-4}
β-NiOOH	*a*, *b*	3.07 Å	0.003	*a*, *b*	2.25 Å	0.002
	c	4.78 Å	0.005	*c*	4.69 Å	0.001
	Microstrain	−0.007	0.01×10^{-5}	Microstrain	−0.028	1.9×10^{-4}

with a low contrast area in the background (Fig. 2c). The upper right inset of Fig. 2c shows the magnified view of the overlapped β-NiOOH layers (1–3), where the thin film morphology of NiOOH is highlighted. The left upper inset (Fig. 2c) is the corresponding SAED diffraction pattern with only a few bright spots, which depicts the low number of layers in NiOOH. In Fig. 2d, the HR cross-sectional views of the MoS_2 interlayer planes (002) are given for the two concentrations of the composites MN-1 (left) and MN-2 (right), respectively, with the histogram plot in the center as analyzed from the IMAGE-J software, showing the quantitative average layer spacing in Å for MoS_2 in the two composites.[47]

For MN-1, the average separation of the (002) MoS_2 layer is about 6.4 Å, which is in good agreement with the typical normal

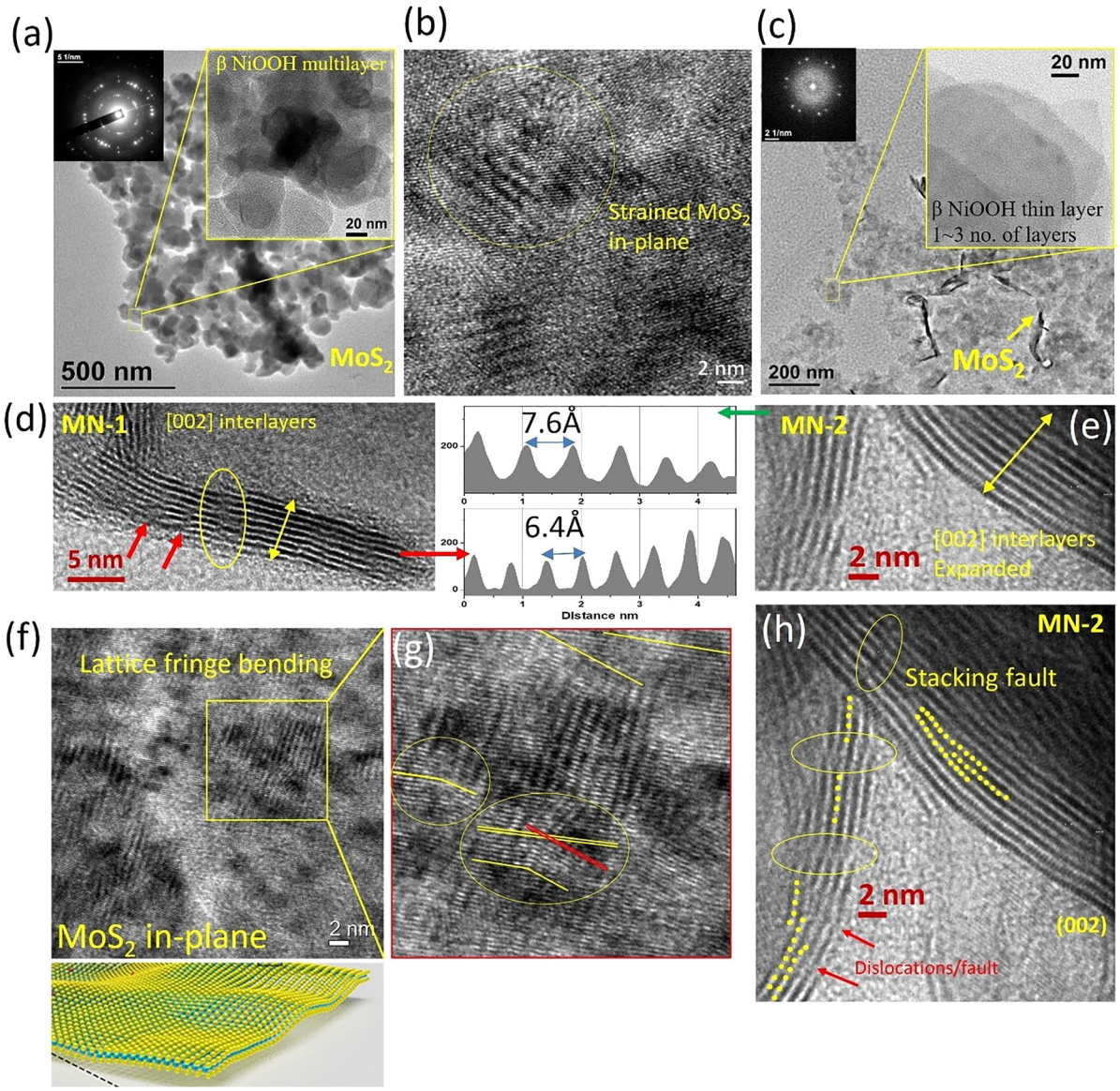

Fig. 2 (a) Overall TEM morphology of the MN-1 composite with the inset showing the overlapped β-NiOOH nanodisc. SAED multispot confirms the layered-type structure. (b) High-resolution magnified view of the highly strained in-plane MoS_2 due to the formation of the heterostructure. (c) Overall morphology of the MN-1 samples with the inset showing the magnified view of the thin layers of the β-NiOOH phase. (d) Left: (MN-1) magnified view of the (002) MoS_2 interlayers with the corresponding plot of the histogram shown in the center. The average peak separation is the interlayer distance between the MoS_2 layers, *i.e.* 6.4 Å. (e) Right: For the MN-2 composite, the (002) interlayers are expanded (7.6 Å) with the corresponding histogram plot in the centre. (f) In-plane lattice fringe bending of the composite with waving of the layers. (g) Magnified view of the in-plane structure shows the local lattice distortion due to the strain and bending in the fringes, and growth in different orientations. Local dark patches verify the strain effect in MoS_2. (h) Overall view of the MN-2 cross-sectional (002) plane with the stacking fault and dislocations/faults highlighted by yellow circles.

2-H type MoS_2-layer spacing of 6.45 Å.[48] Whereas, for the MN-2 nanocomposite, MoS_2, the interlayers are expanded, and the average interlayer separation comes to 7.6 Å due to the high out-of-plane uniaxial tensile strain generated (along the [001] direction) in the hybrid structures with much more strain and defects.[49] The (002) plane spacing highly depends on the strain, defects, intercalation or exfoliation. In our case, there is no effect from the intercalation. Hence, the expansion and distortion are primarily due to the strain effect discussed here in detail with more TEM cross-sectional and basal planar microstructural images. In fact, intercalated structures (if any) would have been seen in the (002) planes in the cross-sectional view, which is absent here.[50,51] From the separation between the peaks in the histogram plot of the interlayers (middle figures), it can be understood how the layers are expanded, counting 8 peaks for MN-1 and 6 peaks for MN-2 within a similar uniform lateral distance scale range of (002) planes (middle of Fig. 2(d)).

In Fig. 2f, we show another in-plane high resolution lattice image of the MN-2 composite, where the lattice fringe bending

is sharply observed as a result of the NiOOH growth and strain effect involvement.[52,53] Upon further magnification of the yellow colour highlighted part in Fig. 2g, lattice fringe bending and waviness are observed throughout the in-plane TEM image of the composite, especially near the center. These are indicative of the local in-plane, bi-axial strain and lattice distortion in 2D materials, which may be due to substrate mismatch and interfacial stress due to composite growth.[39] The lattice fringes are clearly bent and formed twinning boundaries, as highlighted in the yellow circled regions (Fig. 2g). In the large view of the cross-sectional image of MN-2 shown in Fig. 2h, there is a fringe compression/expansion showing the non-uniform fringe spacing, which leads to local variation in the (002) interlayer spacing. Dislocation faults in the (002) layers are marked specifically with yellow-colored circles (Fig. 2h), and formed by point defects or vacancy clusters altering the interlayer interaction.[54] This can be interpreted as out-of-plane strain, *i.e.* perpendicular to the (002) plane. Furthermore, edge dislocation or stacking faults are seen among the (002) interlayer planes highlighted with yellow dots as the planes are merged or dislocated, as shown in Fig. 2h. Hence, from the TEM analysis, a clear picture of the overall growth morphology and surface defects are identified in the 2D surfaces, along with the thin nanodiscs as observed in typical microstructural analysis.[52–54]

D. Raman spectral analysis of the vibrational modes of MoS_2 due to strain

MoS_2 exhibits only weak bonds between the stacked S–Mo–S layers, which are held together by the van der Waals' forces.[55] Out of the different atomic vibrational modes in MoS_2, the out-of-plane A_{1g} mode (sulfur atoms move in opposite directions perpendicular to the plane, while Mo atoms remain stationary) and in-plane E^1_{2g} mode (Mo and S atoms vibrate in opposite directions within the plane) are the most active ones. The presence of the foreign β-NiOOH layer can induce strain in MoS_2, which alters the interlayer interaction and changes the characteristics peaks in the Raman spectra. The positions of the E^1_{2g} and A_{1g} peaks for the pristine MoS_2 phase arise at about 382.9 and 407.7 cm^{-1}, as shown in Fig. 3. Compared to this, for the nanocomposites MN-1 and MN-2, a red shift of both E^1_{2g} and A_{1g} modes are observed, which is typically due to the strain generated in the MoS_2 planes, as found in other literature studies as well (SI: Fig. S1a and b).[56,57] From Fig. S1 in SI, the shift in the E^1_{2g} mode is the strongest in MN-2 compared to MN-1 or pristine MoS_2, which is mainly sensitive to the strain effect.[56,57] The out-of-plane tensile strain in MoS_2 weakens the interlayer interaction, leading to a shift in the frequency from the pristine MoS_2 to MN-1 or MN-2, as observed in our case. Furthermore, the difference between these two modes, *i.e.*, $\Delta\omega = A_{1g} - E^1_{2g}$ (in cm^{-1}), remains almost constant in the case of the composites (Fig. S1b). This is due to the fact that the layer number in MoS_2 does not change with the samples. This plot is important as with increasing the number of layers in MoS_2, the E^1_{2g} mode is red-shifted to higher frequency. Furthermore, the difference between A_{1g} and E^1_{2g} is also enlarged, which is not the case here.[29] Hence, the initial layer number

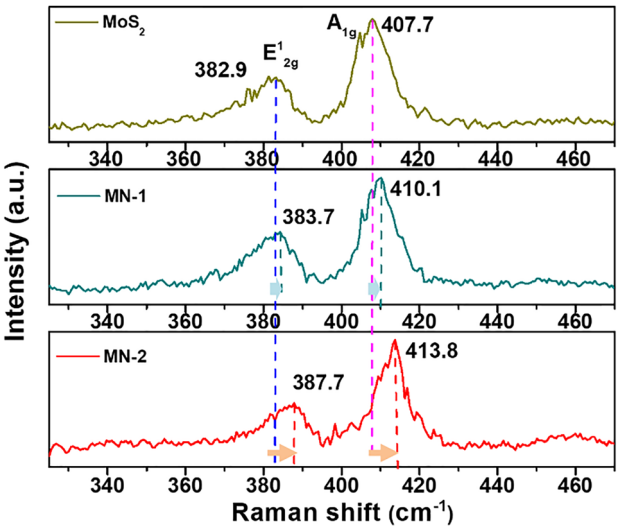

Fig. 3 Raman spectra of the two composites along with the pristine MoS_2 phase for comparison of peak shifting and strain analysis. The position of E_{2g} and A_{1g} are shifted with respect to the pure MoS_2 phase, and the dashed line shows the position with the shift in the composite samples.

in MoS_2 remains the same for the two different batches of samples, as seen from the Raman studies. However, for both MN-1 and MN-2 composites, the characteristic E^1_{2g} and A_{1g} peaks are shifted from the pristine MoS_2 prepared in the same way. The reason for this shift is due to the surface growth of the different NiOOH phases that change the interlayer interaction among the layers in MoS_2 *via* interface interaction. Hence, from the Raman analysis of the two composites along with the pristine MoS_2 phase, the strain effect is evidenced due to the noticeable positional change in the characteristic vibrational modes of MoS_2.

E. Surface topography analysis of the composites by atomic for microscopy (AFM)

Fig. 4a–c shows the contact mode AFM images of the two samples (MN-1 and MN-2) that depict the height profile of the grown nanostructures of the composite. Both samples were measured on the SiO_2/Si wafer as a reference substrate for the AFM measurement with the composite sample drop-casted on the wafer and dried well before measurement. Fig. 4a shows the MN-1 sample and Fig. 4b and c corresponds to the MN-2 samples. In Fig. 4a, a typical β-NiOOH nanodisc is shown on top of a multilayered MoS_2 surface for the MN-1 phase, *i.e.* thick β-NiOOH layers. To accurately measure the height, we have measured several lines (in different colours) and the height profile *vs.* lateral dimension are shown sidewise. In the red and blue profiles for MN-1 (Fig. 4a), a clear step height due to the NiOOH phase is observed over MoS_2 with an average height of about 20 nm. The contrast difference between MoS_2 and the β-NiOOH phase can be clearly understood from the top surface morphology images that also reveal the difference in the height profiles. For MN-1, from the AFM image, we also calculated the average surface roughness and average height of a large specific area from the histogram plot (SI, Fig. S4a). Quantitative analysis

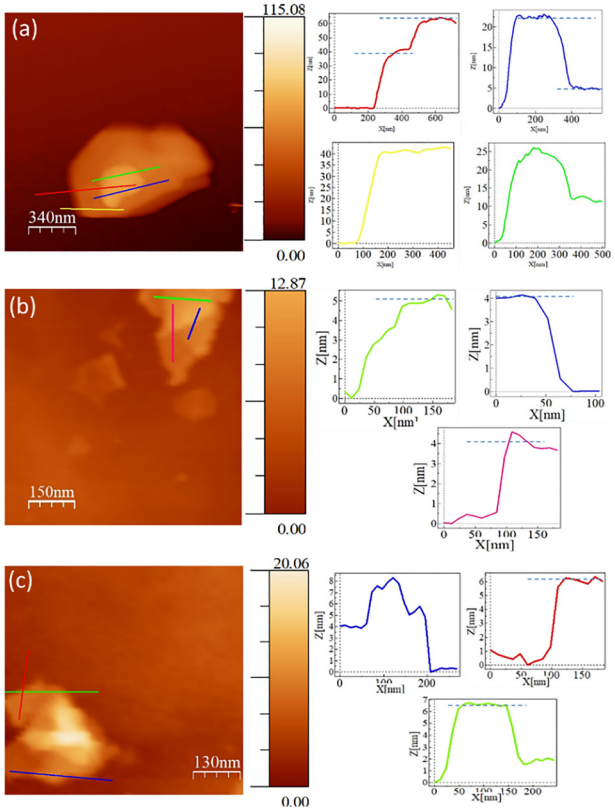

Fig. 4 (a) AFM image of MN-1 with the height profiles of the β-NiOOH layers on the right. The step-like behavior of the typical multilayered heterostructure (MN-1). (b) For MN-2, the thin layer of β-NiOOH can be seen with the average height profile plot shown on the right. (c) For the overall plot of MN-2, with the height profile in the inset showing the average thickness of the grown structures. See SI for the surface topography detailed analysis Section 4.

of the surface roughness was performed by extracting height distribution histograms from the AFM images using WSxM software (see methods in SI, Section S4). From the plot in the histogram (green colour), it is found that MN-1 exhibits an average height of 15.81 nm with a roughness average of 10.64 nm, and a surface skewness of 1.74, indicating a predominantly protruding surface with more high features. A surface kurtosis of 5.17 was found for MN-1, indicating the higher probability of isolated topographic irregularities, consistent with thicker NiOOH nucleation and aggregation. Next, as shown in Fig. 4b and c, thin layers of the β-NiOOH phase with the bottom MoS_2 layer are shown for MN-2 composites, where the number of NiOOH layers are smaller and corresponds to thinner phases. In Fig. 4b, for the MN-2 sample in a selected area, we measured three different line profiles as shown in the green, blue and red colours (on the right side within the height profile plots) and found an average height of 4 to 5 nm of the β-NiOOH phase from the height profile figure. For this plot, we also performed a detailed roughness analysis separately, as shown in SI, Section S4 and Fig. S4(b) with an average height of 3.5 nm from the histogram plot, a surface roughness of 1.39 nm, a surface skewness of 1.89, and a surface kurtosis of 7.81. The corresponding spectrum is shown in blue colour on the right side (SI, Section S4 and Fig. S4(b)). Hence, the MN-2 samples exhibited a much smoother topography, with an average roughness of 1.39 nm and an average NiOOH flake height of 3.51 nm. These values reflect the presence of ultrathin NiOOH layers or clusters sparsely decorating the MoS_2 surface. In another repeat measurement of MN-2 from the same sample (Fig. 4c), the β-NiOOH average height came as ~5–6 nm from the height profile plots in different colored lines. For this image in Fig. 4c, we also performed the roughness analysis (Fig. S4C, in SI) with the histogram indicated in blue colour, an calculated average height of 5.26 nm, an average surface roughness of 1.75 nm, a surface skewness of 2.27 and a surface kurtosis of 10.10. The positive skewness in all of the samples indicates the sharp peaks from the height profiles, *i.e.* topological wrinkles from highly strained MoS_2 layers, dislocation outcrops. On the other hand, kurtosis measures the tailedness or sharpness of the height distribution. Here, a high kurtosis (>3) denotes the presence of sharp features that are often linked to localized strain, defect pinning or out-of-plane distortions.[58,59] The elevated skewness and kurtosis parameters in both samples, particularly in MN-2, suggest the presence of localized strain fields and structural inhomogeneities, likely arising from NiOOH–MoS_2 interfacial interactions.[58,59]

F. X-ray photoelectron spectroscopy of pure MoS_2 and the MoS_2–NiOOH composite for interfacial charge transfer analysis

In the MoS_2–β-NiOOH composite, as MoS_2 interacts with the NiOOH phase at the interface, interesting chemical and electronic interactions such as charge transfer and binding energy change are synergistically detected *via* X-ray photoelectron spectroscopy (XPS) analysis. We have performed a detailed XPS study of the pure MoS_2 and MoS_2 β-NiOOH composite (MN-2 sample) by drop-casting the samples on a Si wafer (see SI, Section S5 for details of the XPS measurement and protocol). Fig. S5 in SI shows the overall survey peaks of pure MoS_2 and the composites, where only the typical Mo, S, Ni, O and Si peaks are observed, proving the purity of the samples.

The high-resolution Mo 3d core level spectra of pure MoS_2 and MoS_2–NiOOH are shown in Fig. 5a with the main dual peaks arising from Mo $3d_{3/2}$ and $3d_{5/2}$ deconvoluted further into two peaks by employing Gaussian–Lorentzian mixing. For pure MoS_2, the main Mo $3d_{5/2}$ and $3d_{3/2}$ peaks appeared at around 229.07 and 232.26 eV, respectively. Meanwhile, for the composite, the main 3d peaks are shifted to 229.69 and 232.90 eV. The shift is due to the interfacial charge transfer from MoS_2 to NiOOH (Mo becomes more electron-deficient). NiOOH is electrochemically active and can act as an electron acceptor due to its oxidative character. Hence, electrons can transfer from MoS_2 to NiOOH, making Mo become more electron-deficient. Also, within each Mo 3d orbital doublet, the i-MoS_2 peak (purple colour) refers to the stoichiometric intrinsic MoS_2 and d-MoS_2 peaks (violet) for defective or sub-stoichiometric parts, denoting vacancies and defects in MoS_2 [ref. 60]. If we compare the XPS Mo 3d spectra of the pure MoS_2 and MoS_2–NiOOH composite, there is a clear reduction in the contribution of i-MoS_2 (purple area) in the composite. Meanwhile, the increase in the contribution of d-MoS_2 (green area) for the

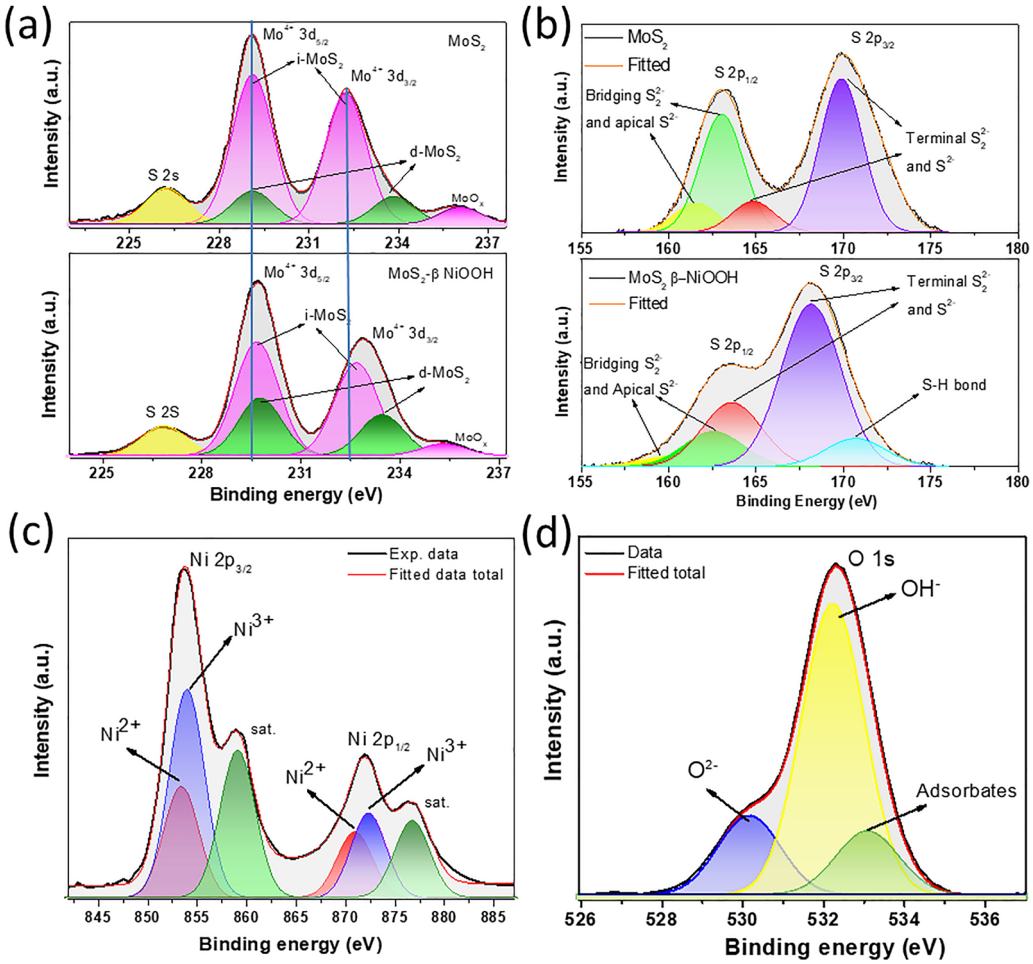

Fig. 5 (a) Mo 3d orbital XPS spectra of pure MoS_2 (top) and the MoS_2–NiOOH composite (bottom) with deconvoluted parts from different components and species with identifications. (b) S 2p orbital XPS spectra of pure MoS_2 (top) and the MoS_2–NiOOH composite (bottom) with the deconvoluted parts inside for different components. (c) Ni 2p orbital spectra for the composite with the deconvoluted components denoting the oxidation state of Ni ions. (d) The O 1s spectrum from the composite with the deconvoluted parts and contribution from the components.

composite is due to more vacancies/defects in the composite.[61,62] The other peak at around 226 eV is due to the S 2s orbital bound to the Mo atom in the structure, which is usually found.

Next, the high-resolution, S 2p doublet spectra ($2p_{1/2}$ and $2p_{3/2}$) from the pure MoS_2 and composite MoS_2–NiOOH phase (shown in Fig. 5b) are further deconvoluted into mainly four peaks. In the case of pure MoS_2, peaks at 164.79 (red colour) and 169.92 eV (blue) are contributed from the terminal disulfur S_2^{2-} or sulfur S^{2-} species. Meanwhile, peaks at 163.05 and 161.54 eV are due to apical S^{2-} or bridging S^{2-} (green and yellow) for the pure MoS_2.[63,64] In the case of the MoS_2–NiOOH composite, the peaks for the terminal disulfur S_2^{2-} or sulfur S^{2-} species are shifted to lower binding energies of 163.59 eV (red) and 168.21 eV (blue) with sharply increased intensity for terminal S. It is known that terminal S_2^{2-} is mainly responsible for the active binding/interfacial interaction sites in MoS_2 and often lower in binding energy whenever it interacts with nearby complexes, as observed in other literature too.[65,66]

On the other hand, the S peaks for bridging and apical are reduced in intensity for the composite sample. As a result, for the composite, the S 2p peaks are shifted to overall lower binding energies.[63] Additionally, for the composite, the peak appearing at around 170.68 eV may be attributed to S–H interfacial bonds, which is found here due to interface interaction.

In β-NiOOH, it contains both Ni^{2+} and Ni^{3+} species. In XPS, these typically show distinguishable peaks in the Ni 2p region (846–890 eV), often with satellite structures (Fig. 5c). It shows multiplet-split peaks due to the interaction between the Ni 2p core and the 3d valence electrons. When MoS_2 interacts with NiOOH, the relative intensities and positions of Ni^{2+} and Ni^{3+} peaks can change, reflecting the charge transfer and oxidation state redistribution, as found in Fig. 5c for the Ni 2p peak of the composite.[67,68] After deconvolution of the 2p spectra ($2p_{3/2}$ and $2p_{1/2}$), the majority of the intense peaks at around 854.07 and 872.18 eV are due to the Ni^{3+} species in the NiOOH phase, while the lower binding energy peaks at around 853.42 and 870.81 eV are due to the Ni^{2+} species, due to the presence of a partial $Ni(OH)_2$ phase and reduction by the interfacial charge transfer effect transforming a part of NiOOH to $Ni(OH)_2$.[69,70] The Ni satellite peaks are also detected at around 860 and 876 eV

(green colour), which are usually observed in the Ni 2p spectra. Next, the O 1s spectrum from the composite is shown in Fig. 5d. When deconvoluted, it appears to be multiple components, where the main highly intense peak at around 532.21 eV (yellow) is due to the OH^- group from NiOOH, the small peak at around 530.15 eV is due to the lattice O^{2-} which is correlated to the Ni–O lattice in NiOOH/$Ni(OH)_2$ that occurs due to partial reduction as a result of charge transfer, with the additional adsorbate peak at a higher binding energy of 533.1 eV. Hence, in summary, XPS analysis of the MoS_2–NiOOH heterostructure reveals clear evidence of interfacial interaction and charge transfer from MoS_2 to NiOOH, accompanied by shifts in core-level binding energies and the presence of mixed Ni^{2+}/Ni^{3+} states. Additionally, subtle changes in the S 2p region suggest defect formation, contribution from different intrinsic (less defective) MoS_2 and defect-rich MoS_2 as a result of composite growth and electronic modulation within the orbital binding energy due to interfacial interaction.

3. Magnetic measurements

A. Spontaneous magnetization curves of the MoS_2-based hybrids

To understand the intrinsic behavior of the hybrid systems, we carried out zero field cooled (ZFC) and field cooled (FC) magnetization protocols under different dc magnetic fields in the temperature range of 2–300 K in a MPMS superconducting quantum interference device (SQUID) magnetometer, as shown in Fig. 6. For both samples, large exchange splitting has been observed between the FC and ZFC branch up to a temperature of 300 K, proving the strong magnetic ordering in the hybrid system compared to the pristine MoS_2 phase, where it was absent (see SI, Fig. S2). For the thick coverage sample (MN-1), the characteristic antiferromagnetic ordering appeared in the ZFC curves at around 50 K, which becomes stronger with increased magnetic field (inset of Fig. 6a). At 100 Oe field, the peak in ZFC was not sharp, so we increased the field strength. At 500 Oe, the change becomes more prominent and visible. In the low temperature region, for MN-1, the FC branch did not become completely saturated due to the presence of stronger antiferromagnetic ordering (at low temperatures) among the overlapped β-NiOOH clusters in the Z direction (vertical to the in-plane MoS_2). From the first-order derivative plot of $\Delta(M_{FC} - M_{ZFC})$ (*i.e.* difference between the magnetizations) in Fig. 6b, the ordering temperature (which is T_N in this case) is estimated to be 52 K for the 500 Oe field. The inset of Fig. 6b shows the full variation of $\Delta(M_{FC} - M_{ZFC})$ *vs.* T with a prominent point of inflection around this temperature. As we tuned (reduced) the thickness of the β-NiOOH phase over MoS_2 in the MN-2 sample, the exchange splitting has enormously increased with complete saturation in FC magnetization throughout the temperature

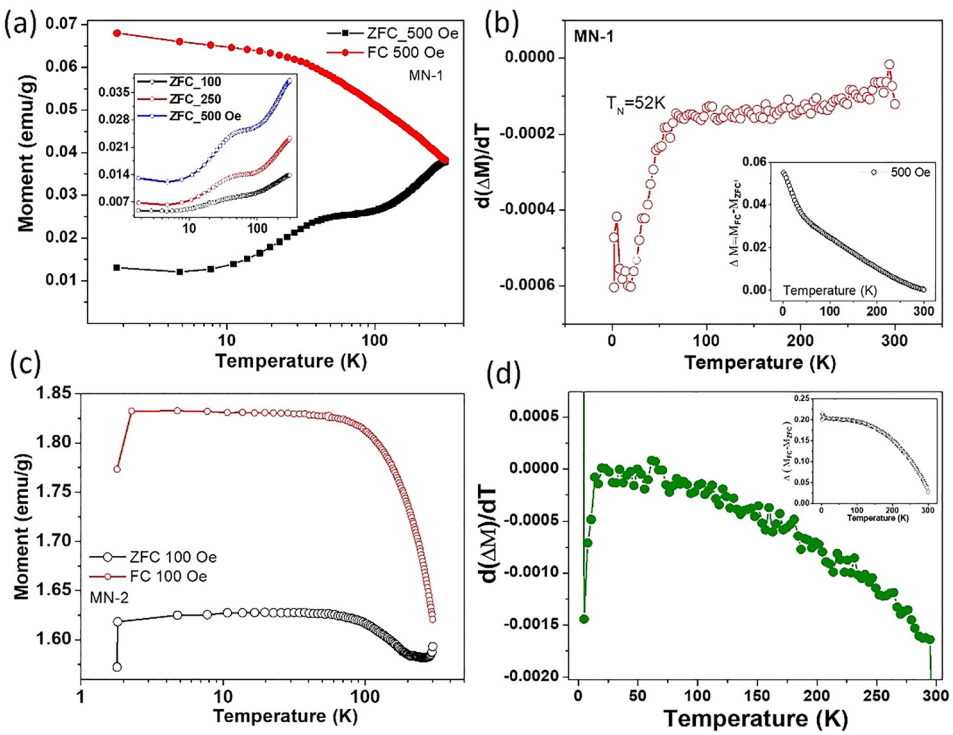

Fig. 6 (a) ZFC–FC plot of MN-1 during the heating cycle. The inset shows the effect of increasing magnetic fields on the ZFC curves. (b) First order derivative plot of $\Delta M(M_{FC} - M_{ZFC})$ with respect to temperature, showing the point of inflection at 52 K. The inset shows the original difference plot as a function of temperature for MN-1 obtained from the ZFC–FC plot. (c) ZFC_FC plot for MN-2 with complete saturation at low temperature due to strong ferromagnetic ordering. (d) Corresponding derivative plot of $\Delta M(M_{FC} - M_{ZFC})$ for MN-2. Inset showing the original difference plot from the ZFC_FC curve of MN-2.

range of 100 K due to stronger ferromagnetic ordering in the system (Fig. 6c). The $\Delta(M_{FC} - M_{ZFC})$ *vs. T* curve (inset of Fig. 6d) shows a uniform variation of up to 300 K. Interestingly, the specific magnetization moment of the hybrid composite has increased by many folds in the MN-2 phase, which points to induced magnetization in the MoS_2 phase, in addition to the weakly magnetic β-NiOOH phase. For MN-2, at the lowest temperature point of 2 K in the ZFC_FC plot, the data point was lowered. This may be due to the stabilization effect of SQUID and can be neglected.

B. Coupling of interfacial magnetic phases resulting in two-step magnetization and giant exchange bias in the hybrids

The tuning of the diamagnetic or weakly paramagnetic MoS_2 into a giant coercive material has been achieved by ultrathin AFM layers of the β-NiOOH phase. For this purpose, we measured the ZFC MH hysteresis loops of the two samples in ±5 T magnetic field with a field ramp rate of 100 Oe s^{-1}. The low temperature (1.8–20 K) data (Fig. 7a) resemble a strong antiferromagnetic phase, along with charge-transfer-induced FM phase arising from the interfacial MoS_2 layer that did not let the magnetic moment saturate even until application of the 5 T strong field. The interlayer exchange coupling (IEC) arises due to the overgrown, thick AFM β-NiOOH layers interacting with the MoS_2 sheet, which is still present in the low field region of the HC sample (inset of Fig. 7a). Moving to the high temperature region (100–300 K), observation of the ZFC exchange bias with the temperature-driven antiferromagnetic spin canting at the surface is noticed in the disordered surface, and defects of MoS_2 can lead to such high coercive fields. Quantitatively, the average coercive fields are evaluated here, by the following formula:

$$H_C = (|H_C^+| + |H_C^-|)/2$$

where $|H_C^+|$ and $|H_C^-|$ are the magnitudes of the positive and negative bias coercive fields in Oe, respectively. This is defined as the half-width of the MH loop at the average of the zero field intercepts, and $\langle H_C \rangle$ represents a non-trivial dependence with temperature (inset of Fig. 7b). The strength of exchange bias is calculated by:

$$H_{EB} = (H_C^+ + H_C^-)/2,$$

where the polarity of the field is also considered. It is interesting to note that the ZFC exchange bias becomes the maximum value at around 70 K with a large magnitude of −1527 Oe, which is an astonishingly high value for any MoS_2-based 2D hybrid system made so far. Upon increasing the temperature (around 300 K), it gradually approaches zero due to the high thermal agitation near room temperature. This behavioral observation becomes clearer if we plot the isothermal $\partial M/\partial H$ *vs. T*

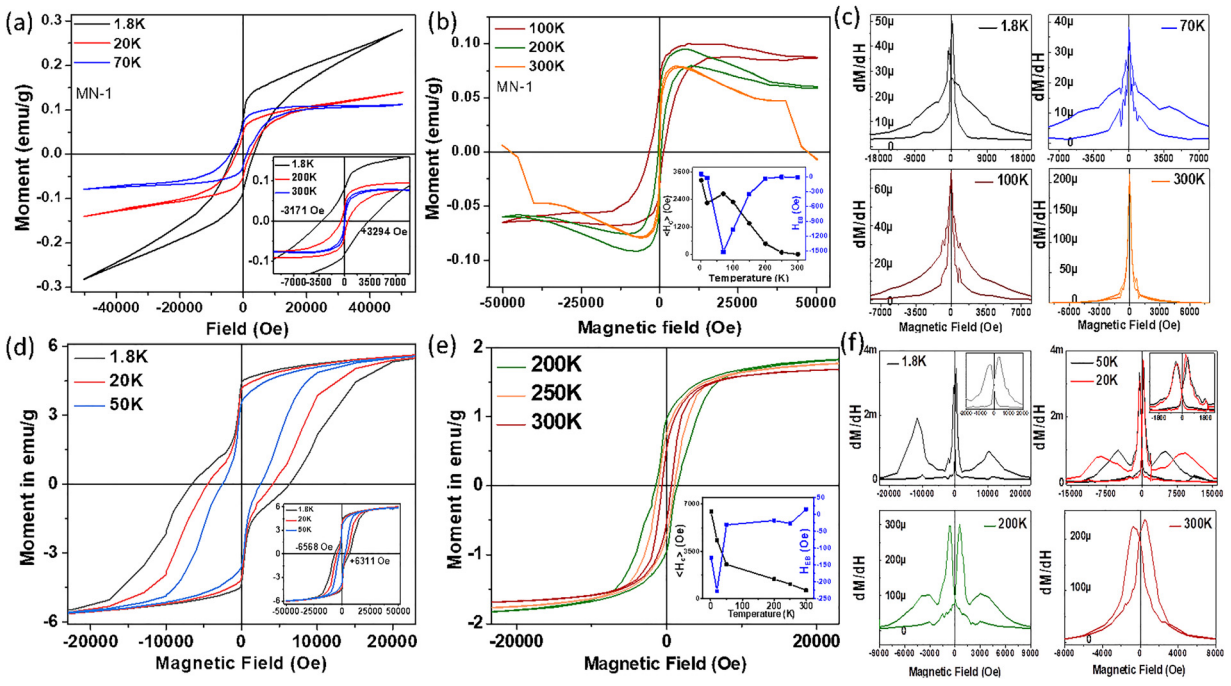

Fig. 7 (a) MH hysteresis loop for MN-1 in the low temperature range. Inset showing the magnified loops near the zero-field region. (b) MH loop for MN-1 in the high temperature region with a strong interlayer exchange effect, which gives the waist restricted hysteresis loop. The inset shows the variation of the average coercivity (H_C) and exchange bias (H_{EB}) with temperature for MN-1. (c) The dM/dH plots at different temperatures to understand the interlayer exchange effect (splitting near the zero field region). The IEC effect is the maximum at 70 K for MN-1. (d) MH hysteresis loop for MN-2 at low temperature with the inset showing complete ferromagnetic saturation at higher fields. Two-step magnetizations can be viewed from the nature of the curve. (e) High temperature hysteresis loop. Inset depicts the variation of $\langle H_C \rangle$ and H_{EB} with temperature in this case. (f) The dM/dH plots at different temperatures. The clear asymmetric nature and two peaks are observed due to FM–AFM coupling and two-step magnetization process. Unlike MN-1, here the splitting exists until 300 K due to the evolution of very strong ferromagnetic ordering in the heterostructure.

for HC at different temperatures (Fig. 7c). The strong asymmetric derivative plot@1.8 K shows the large exchange correlations, witnessing butterfly-like splitting near the low bias fields. With the rising temperature, a component of the canted AFM spin (from the β-NiOOH phase) rises and ZFC EB becomes the strongest at around 70 K, which is also near the transition temperature of the HC sample (MN-1).

Recently, it has been found that surface-pinned uncompensated moments at the FM/AFM interface play a dominant role in generating exchange bias and its magnitude.[71–74] When the AFM layer is thinned down over the 2D surface, what change occurs is evident from the MH loop of sample MN-2 (Fig. 7d). At the lowest temperature of 1.8 K, an enormous average coercive field $\langle H_C \rangle$ of 6439 Oe has been achieved from an ultrathin AFM layer of the β-NiOOH/MoS_2 interface. The saturation nature of magnetization at the highest 5 T field represents an overall strong FM ordering in this phase, which is confirmed by fitting the initial growth of the magnetization data with the law of approach to saturation magnetization (LAS) in this case [Fig. S3 in SI]. This strong spin exchange coupling between the itinerant AFM layer and charge transfer-induced FM order parameter produces this large coercive field in such composite system. In addition to this, the defective, highly strain-induced MoS_2 layers act as robust pinning sites of the surface-canted spins. As a result, two step magnetization curves have been found prominently in the lower temperature range of MN-1.[74] As the epitaxial strain in MoS_2 for the thin β-NiOOH phase is larger, the charge transfer-induced FM phase is additionally supplemented by the surface-pinned AFM states. We have exploited the interfacial magnetism by virtue of the epitaxial strain, charge transfer hybridization and defects, *etc.*,[75–78] while in the case of the thinner phase, this two-step magnetization is sustained until 200 K (Fig. 6e), above which the thermal energy weakens the interaction. The natures of variation of E_B and H_C with temperature are given in the inset of Fig. 7b and e.

The presence of coexisting soft and hard magnetic phases (independent) can, in some systems, lead to such two-step magnetization behaviour. However, to further verify whether interfacial exchange coupling plays a dominant role in our system, we also performed field-cooled (FC) MH measurements for the MN-2 sample at 1.8 K, as shown in SI, Fig. S6. As depicted in this figure, the FC MH loop for MN-2 exhibits a clear horizontal shift with respect to the zero-field axis, which is a characteristic signature of the exchange bias. This shift directly confirms the presence of interfacial exchange coupling between the ferromagnetic (FM) MoS_2 phase and the antiferromagnetic (AFM) β-NiOOH layer, rather than the independent behaviour of soft and hard magnetic phases. If the double hysteresis loop originated purely from coexisting soft and hard magnetic regions with no interfacial coupling, the FC M–H loop will not exhibit an exchange bias shift. Field cooling has induced unidirectional anisotropy, pinning the AFM surface spins, resulting in a horizontal shift of the FC MH loop.

The asymmetry in the positive and negative field-bias can be clearly observed in the $\partial M/\partial H$ plot for MN-2 in Fig. 7f. Two prominent peaks appear near the low bias field only in the derivative plots, which exist up to 200 K. At 300 K, there is only one large splitting that is observed due to the high thermal energy.

The induced ferromagnetism in our system predominantly originates from interfacial exchange coupling between the weakly antiferromagnetic β-NiOOH and MoS_2. In the MN-2 sample, where the β-NiOOH layer is very thin (~3.5–5 nm), the interface is more exposed, enhancing the proximity effect and leading to stronger interfacial magnetization. In contrast, the thicker β-NiOOH layer in MN-1 (~20 nm) results in weaker interface contribution due to partial screening. However, our XRD and strain analyses (Fig. 2 and Table 1) reveal significant out-of-plane uniaxial tensile strain in MoS_2, especially in MN-2, which alters the interlayer spacing and modulates the spin interactions beyond just the interface. Thus, while the magnetism is primarily interfacial, strain-induced changes in the MoS_2 structure also contribute, making the overall MoS_2 thickness relevant to the observed magnetic properties.

4. Thermoremanent-magnetization memory effect studies

A. Thermally induced read/write memory states in MoS_2 based hybrids

The presence of the high exchange bias and coercivity in the 2D hybrid composite suggests the possibility of a memory effect due to the strong interaction among the magnetic nanoclusters.[79,80] To verify this, we have investigated in detail a set of measurement protocols for defining the memory states. At first, the MN-2 sample is field-cooled (200 Oe) from 300 K at a constant cooling rate of 2 K min^{-1}. In the temperature range from 70 K to 10 K, at 20 K intervals, the field is kept off for t = 1 h to create temporary memory steps (fall) in the magnetization process. This can be equivalent to a 'writing' process in the system. At designated temperatures, it is possible to create such steps and each level of state represents each value. During this wait time (t_w), the magnetization relaxes downward as the field is switched off. After 1 h, the field is switched on again and cooling continues until further steps are reached. By measuring in this way, we obtained a cooling curve until 1.8 K (blue color curve in Fig. 8a). After reaching 1.8 K, the cycle is completed by heating continuously at the same rate without halting at any intermediate temperature (red curve). Surprisingly, the return magnetization (heating process) also follows the same steps created at the particular exact temperatures during cooling. This tracing can be compared to the 'reading' effect in the memory process. By just scanning a thermal scan with a low field, the states can be read. This temperature-based magnetization state is called the thermoremanent memory effect, which is newly achieved for 2D hybrid systems by interfacing AFM ultrathin layers. It should be noted that, in contrast to the field, which is usually a control parameter for memory, thermal energy is used here to embed and trace the memory effect in these hybrid heterostructures.[81,82]

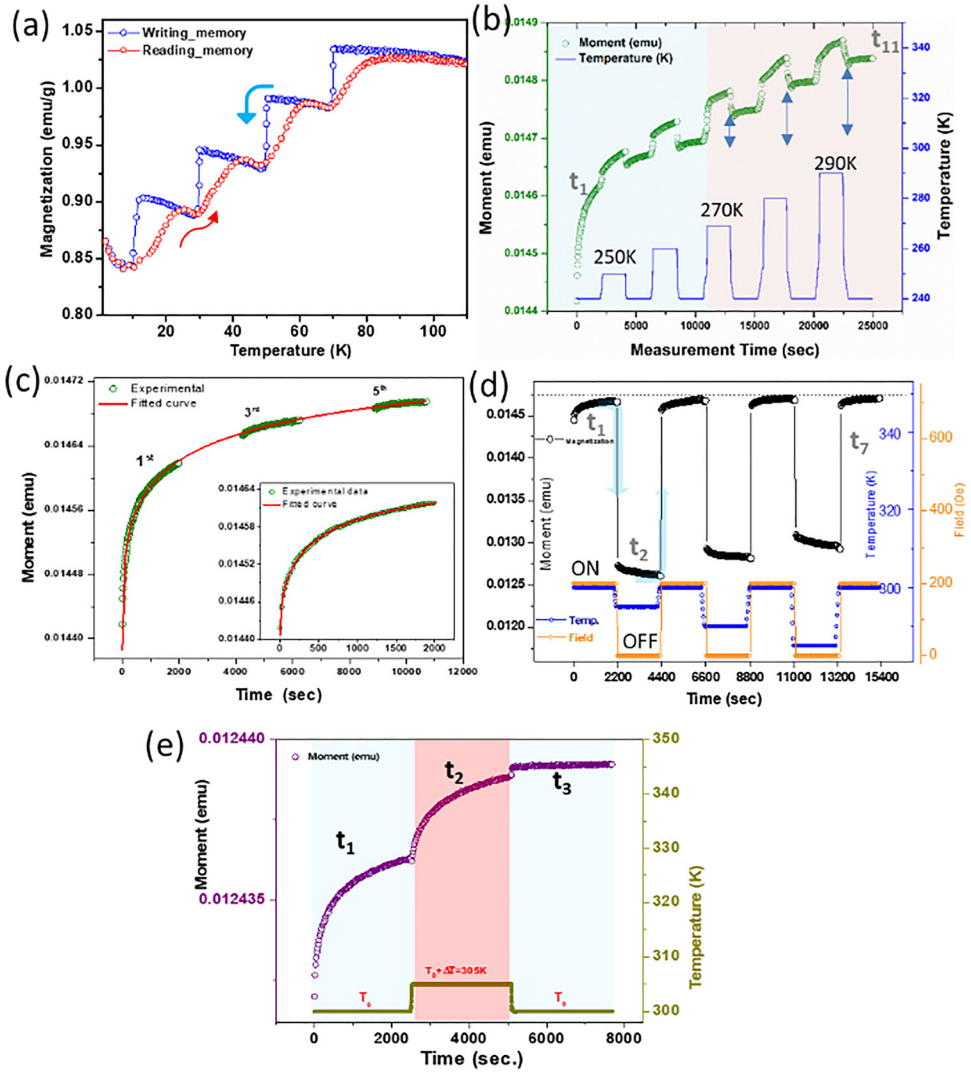

Fig. 8 (a) Magnetization memory writing–reading process during the cooling heating cycles in steps, (b) long relaxation with the temporary heating process with increasing temperature. Despite the positive thermal cycle, the memory effect is sustained until 270 K. (c) Fitting of independent odd thermal cycles with unique stretched exponential curves. Even after intermediate halts, the graphs can be fitted uniformly. The inset shows a complete fit for one cycle with this equation. (d) Simultaneous effect of field on/off and variable temperature ramping on the cycles. The level quickly reaches back after the initial condition is retraced back. A total of 7 cycles are performed in this case. (e) Re-initialization of memory states by temporary heating process in 3-time domains. By this manner of heating process, memory can be erased.

B. Fitting of magnetization dynamics in a long relaxation process under different perturbations

To understand the origin of memory dynamics of this hybrid system, it is important to measure the long relaxation process. For this, the sample is ZFC cooled from 300 K at a cooling rate of 2 K min^{-1} and reaches 240 K, which is set as the base temperature here (T_0). A low magnetic field of 200 Oe is applied, and the time evolution of magnetization is recorded initially for 2000 s (t_1). After t_1, the temperature is quickly heated to 250 K (T_0 + ΔT) and magnetization continues for another 2000 seconds (t_2). After this, the initial temperature T_0 is kept back and t_3 continues. In this way, we ramped up the temporary heating and retraced back for 11 cycles (t_{11}), as shown in Fig. 8b. Every time, the temperature is increased for 20 K increments and returned back to 240 K (T_0). Soon after switching on the field, the magnetization grows exponentially up to t_1. During the intermediate time t_2, as the temperature is changed (ΔT), the level of moment independently changes with relaxation. As soon as the initial temperature T_0 is achieved, the moment-level returned to the same value before the temporary heating. Interestingly, t_3 is a continuation of t_1 and found to be independent of t_2. It is pertinent to mention that as time passes, the value of ΔT is enhanced. From t_6 onward, even after returning to T_0, the levels did not match (differentiated by two colour regions), and large thermal ramping deletes the memory states (re-initialized). For conventional thermoremanent materials, even small positive temperature cycling destroys the memory effect. However, due to the robust exchange coupling in this MoS_2-hybrid system, it withstands the positive temperature cycling in the 240–270 K temperature region.

For a more detailed approach, we fitted magnetization dynamics as a function of time by stretched exponential behavior, as follows:[67,68]

$$M(t) = M_0 - M_r \exp\left[-\left(\frac{t}{\tau}\right)^{\beta}\right] \quad (1)$$

Here, M_0 is the temperature-independent ferromagnetic component, M_r is the remanent magnetization and τ is the relaxation time. The 'interaction parameter' β lies between 0 and 1. We used this equation to fit the relaxation process for the time periods of t_1, t_3 and t_5 in the same time scale. Even after forced temporary heating, the magnetization from different time zones follows the same curve as the initial condition (T_0) is achieved (Fig. 8c), *i.e.* t_5 is a continuation of t_3 and t_1. The inset of Fig. 8c shows the fitting of t_1 with eqn (1). The parameters obtained from this fitting also match well for the 3 time zones despite their intermediate different parameter conditions.

C. Simultaneous effect of the temperature and field-ON/OFF on the memory states

To further test the strength of the memory state, we also performed opposite forced relaxations by switching the magnetic field ON or OFF during the temporary cooling period ($T_0 - \Delta T$). This is to perform a large jump in the magnetization level from the initial value (T_0) by ΔT through switching off the field strength ($B = 0$) and letting the system relax in the opposite direction (Fig. 8d). This is done at 300 K to test the room temperature applicability of the samples for practical applications. At the initial condition, *i.e.* $t = 0$, the field is set on so that the initial moment rises to magnetize the spins in the external field direction for a time period t_1 (2200 s). After then, a large jump occurred due to $B = 0$ and relaxes for another t_2 (2200 s) in the opposite direction. Despite such a large jump in the magnetization (large dips in the magnetization plot), when the initial conditions (*i.e.* T_0, B values) are re-applied, the magnetization level quickly reaches its previous value and continues to grow exponentially following the same path of t_1. We continued the temporary cooling (($T_0 - \Delta T$)) for 7 consecutive cycles (257 h, *i.e.* for long 11 days) and the memory level was exactly matched every time, proving the stability and robustness of the sample-memory over time and cycles. Hence, the effect of temporary cooling on the sample is to strengthen the memory irrespective of the external field dependency. This experiment also shows the robustness of the hybrid against external field conditions in terms of cyclability and stability.

D. Re-initialization of the memory states (erasing effect)

So far, the history of magnetization has been preserved by temporary cooling, as discussed in the previous experiments. Now, to erase the memory state, we have performed positive thermal cycling ($T_0 + \Delta T$), where T_0 is set as 300 K and ΔT is just 5 K increment, in a quick manner to reset the initial conditions, which can be similar to erasing the memory from the system. As shown in Fig. 8e, during t_1 (2500 s), the growth of the magnetization is first recorded (purple curve). Then, the temperature is quickly changed to 305 K and magnetized independently for t_2 (2500 s, red region), and finally quenched back to T_0 = 300 K continuously until t_3. Unlike temporary cooling in the previous section, here the level of magnetization and the nature of variation did not match even when the sample returned to the initial conditions. Hence, t_3 is not a continuation of t_1 in this case and completely independent, which is related to re-initializing the memory states. The result of a small positive thermal cycling event is to re-initialize (delete) the memory states, which can be compared to the erasing process in memory devices. With a small thermal agitation at this elevated room temperature, the prehistory is deleted, and the process of magnetization follows a different path.

5. Transport studies of the MoS_2/β-NiOOH junction as a non-volatile charge-memory device

A. Re-writable *I–V* characteristics of the hybrid

To test the capability of the composite as an electrical non-volatile memory device, we have used this material as an active channel layer in a vertical junction-type architecture.[83–85] As shown schematically (Fig. 9a), the ITO-coated substrate was used as the bottom electrode over which a thin uniform layer of the MoS_2-based hybrid was coated (see inset of Fig. 6a for the design). We used the commercial Ag paste as the top electrode with a working area of 2 mm^2. The switching behavior of the electrical properties of the formed structure is shown in the current density *vs.* voltage curve (*J–V*) plot in Fig. 9a. Near the zero bias, the device initially shows low conductivity due to its OFF state (sweep 1). The current density increases with the applied bias, but remains in the OFF state until the threshold voltage (V_{th}) reaches +1.36 V, at which the current density increases abruptly and jumps to the ON state (sweep 2). This step can be represented as an electrical ''writing process'' in the device. The ON state continues during sweeps 3, 4 and changes bias to the negative side until −1.37 V, where the high conductivity state is switched back to the low conductivity OFF state (sweep 5) and can be related to the so-called ''erasing process''. Upon further increasing the negative bias until −1.7 V, the OFF state remains stable (readable) and sweep 6 is completed back to 0 V. During cyclic bias, these ''write/read/erase'' steps are reproduced stably as observed in the cyclic curves. It should be mentioned that we performed the experiment both under zero applied magnetic field (black curve) and 0.5 T field (red curve). The ON/OFF threshold voltage and consequently the ON/OFF current ratio are both found to be dependent on the external magnetic field. For the zero magnetic field, an ON/OFF ratio of ~94 was achieved, increasing to ~600 at 0.5 T, which is quite large for 2D MoS_2-based devices made so far. The initial V_{th} was reduced from 1.36 V to 1.28 V with an application of the 0.5 T field. The strong dependence of these parameters led us to investigate the conductivity variation with the magnetic field, *i.e.*, magnetotransport behavior, which is given later. To check the stability of the current densities in

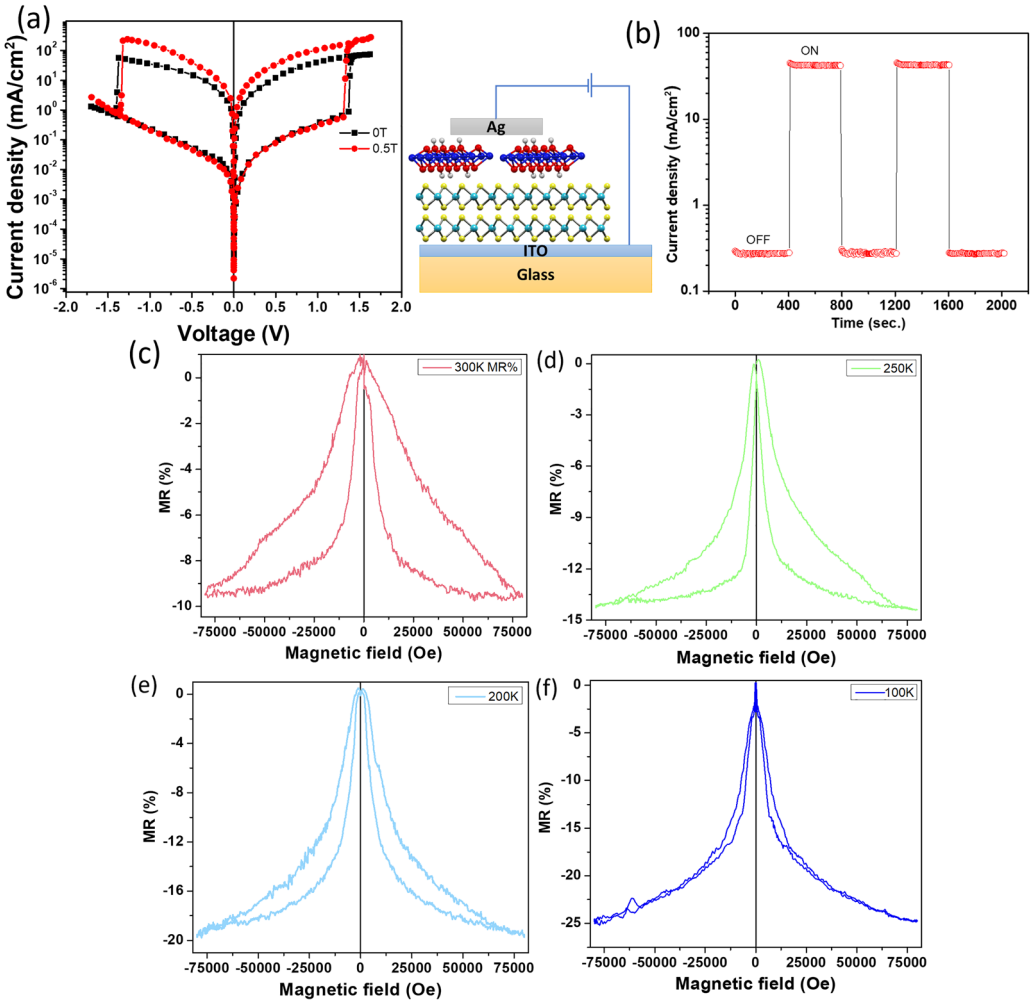

Fig. 9 (a) Current density *vs.* voltage curve at different magnetic fields of the sandwich structure made of the composite samples. (b) Switching behaviour of the ON/OFF state for a complete cycle. (c)–(f) Magnetoresistance curve of the composite measured at different temperatures starting from 300 K to 100 K. Hysteresis is formed during the sweep of the magnetic fields.

the OFF and ON states, we ramped the voltages during these states in a cyclic manner, as shown in Fig. 9b. The first OFF state current density was measured at +0.7 V, and then the ON state value was recorded for another time period. In this way, we changed the states and the cyclic stability was measured. From the figure, it was found that the stability was quite good in the context of the precise switching.

These enhancements likely stem from the magnetic field-assisted modulation of the interfacial spin-charge interactions, which in turn affect the carrier mobility and trap-mediated conduction pathways within the hybrid layer. Therefore, magnetic field tuning provides an additional control knob to engineer lower operating voltages and sharper memory state separation, marking a promising route toward multifunctional spintronic memory elements.

B. Room temperature large hysteretic magnetoresistance of the hybrid heterostructures

To understand the role of the magnetic state of the two different phases in the conductivity of the overall composite, we measured the magnetoresistance of the device in the 2-probe method with application of a magnetic field at different temperatures. The percentage change of the magnetoresistance (%MR) was calculated using the following formula:

$$\%\mathrm{MR} = \frac{\rho(H) - \rho(0)}{\rho(0)} \times 100$$

where $\rho(H)$ and $\rho(0)$ are the resistivities of the composites in the presence and absence of the magnetic field H, respectively. Starting from 300 K (Fig. 9c), the negative magnetoresistance is observed with a hysteresis when the following magnetic field cycling is performed. First, the field is increased from 0 Oe to a maximum of +75 kOe. When it returned to 0 Oe, the resistivity followed a different path (lowered value). When the polarity of the field is changed, *i.e.* 0 to −75 kOe, the change is almost symmetric with the hysteresis loop. The MR% with decreasing temperature increases from 9.4% (300 K) to 25.1% (100 K) (Fig. 9c–f), but the hysteresis disappears almost at 100 K (only existing near zero field regions). As MoS_2 is a diamagnetic/nonmagnetic material,

the observation of the 25% MR value with a huge hysteresis is immensely applicable for spintronics applications. Previously, there was a report of a negative MR effect (−12.7%@90 kOe) in thin layer MoS_2 gated with $CoFe_2O_4$ (CFO), which has a strong ferromagnetic/ferrimagnetic phase.[86] However, in this report, the vanishing of MR occurs when the layer number is increased. In our case, the pristine β-NiOOH is weakly antiferromagnetic in nature, and when adsorbed to MoS_2, it gives a large hysteretic MR even at 300 K. Considering the fact that MoS_2 has overall good semiconducting conductivity and the β-NiOOH phase is an insulator (dielectric), this will not divert the electrical current away from MoS_2. The MR effect in this case may have originated from the proximity-induced magnetism in the MoS_2 layer by the nearby magnetic insulator of the β-NiOOH phase. This effect is highly dependent on the interfacial magnetization of the heterostructure.

The important part is that MR% becomes larger at lower temperatures, but the hysteresis loop is the maximum at 300 K. The essential hysteresis in MR is the manifestation of the dependence of the magnetic state with the itinerant conduction electron. Earlier, some weak hysteresis was reported in rare earth manganites.[87,88] However, in those cases, the low temperature occurrence of hysteresis was explained by spin-dependent tunneling across the dielectric spacer or the formation of ferro–antiferro–ferro tunnel contacts. From our case, the magnetic study already revealed induced magnetization in MoS_2 by the weak AF β-NiOOH phase. Hence, in our case, the inter-granular tunneling can be approximated by the layer surface model, where the ferromagnetic (induced) and antiferromagnetic phases are separated by the anti-phase boundary (APB).[89,90] At a fixed temperature, when the magnetic field is applied (0 to H_{max}), the surface spins (in β-NiOOH) are pinned according to the nearer spins of the FM grains (MoS_2), hence reducing the resistance of the system as an ordered system faces less scattering. While the field is lifted off (H_{max} to 0 Oe), the surface spins remain pinned to the nearest moment of the inner layer, so the return path follows a hysteresis. With the decrease in temperature, the effect of the surface spin fluctuation is diminished and a short-range ordering is formed among the surface spins (cluster formation).[91,92] At lower temperature, the cluster or disordered spins diminish the possibility of spin pinning at the surface and the hysteresis area eventually decreases. It should be noted that due to the semiconducting nature of the MoS_2–NiOOH composite, the resistance of the sample increases significantly at temperatures lower than 100 K. As a result, the resistance level at these temperatures exceeded the measurable limits of our standard PPMS system in the two-probe configuration, preventing reliable MR measurements below 100 K. Despite this, we have provided robust MR data down to 100 K and detailed magnetization data to highlight the evolution of the magnetic behaviour at low temperatures, which still allow for a meaningful qualitative correlation between the structural, magnetic ordering, and magnetotransport effects.

6. Density functional theory (DFT) calculations of the MoS_2/β-NiOOH composite

A. Computational details

The first-principles calculations were performed with the VASP code.[93] We used the projected augmented wave (PAW) method.[94] For the exchange and core-functional, we used the Perdew–Burke–Ernzerhof (PBE) functional.[95,96] The plane wave energy cutoff was set to 400 eV. The dispersion correction was included *via* the Grimme's D3 (BJ) method.[97] The length of the surface lattice vector of the hexagonal MoS_2 and β-NiOOH cell is 6.38 Å and 5.62 Å, respectively, which has a 12% mismatch. To construct the composite, we expanded the β-NiOOH cell to match the MoS_2 cell. The thickness of the vacuum layer is more than 20 Å. The *k*-point was sampled by a gamma-centered $2 \times 2 \times 1$ grid. All the atoms were optimized until the force became smaller than 0.01 eV $Å^{-1}$. We performed DFT calculations to elucidate the spin state of the MoS_2/β-NiOOH composites. The β-NiOOH monolayer and bilayer were optimized on the MoS_2 sheet, as shown in Fig. 10. The computational details can be found in the SI.

It is known that the antiferromagnetic state is stable for the bulk β-NiOOH.[98] The bilayer β-NiOOH on MoS_2 also showed an antiferromagnetic ground state in this case. However, the monolayer MoS_2 showed a ferromagnetic ground state, where the β-NiOOH sheet is spin-polarized. This spin polarization induces a small spin density on MoS_2, indicating the emergence of the 2D ferromagnetism. Furthermore, the Bader charge analysis tells us that 0.03*e* was transferred from MoS_2 to β-NiOOH, which is consistent with the X-ray structural analysis.

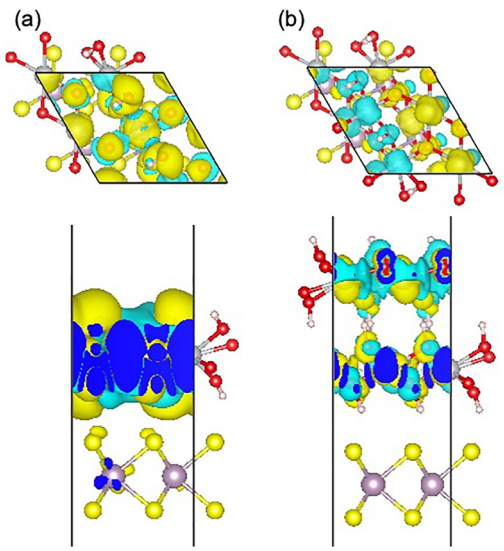

Fig. 10 Top and side views of the spin density distributions of the (a) monolayer β-NiOOH on MoS_2 and (b) bilayer β-NiOOH on MoS_2. The purple, yellow, grey, red and white balls represent Mo, S, Ni, O, and H, respectively. The black line represents the unit cell boundary.

7. Conclusion

In contrast to the classical exchange bias as typically found in the FM/AFM interface, where uncompensated moments are localized and pinned by the AFM surface phase, here we intertwined the weak AFM phase with the layer-dependent 2D MoS_2 surfaces by creating a flat interface. By tuning the thickness of the AFM β-NiOOH phase on top of the 2D MoS_2, a competition between the interfacial effect (surface) and bulk structure (depth) is created, which enables a long-range magnetic exchange interaction in the hybrid heterostructures with a large ZFC exchange bias (1500 Oe) and large coercive field (6439 Oe) in the 2D MoS_2-based heterostructures in a new way. The spin interaction model is described by the presence of an excellent thermally stable, thermoremanent memory effect in this hybrid structure, which shows robust memory states that are easily controllable by temperature, rather than conventional magnetic field intensity or polarity. The localized spin moments from the weak AFM counterpart scatter with the conduction electron of the 2D spacing layer (here MoS_2) and give rise to a hysteretic MR effect of about 25% during charge transport, which could be useful in 2D-based spintronics applications. Furthermore, the non-volatile electrical memory effect strongly persisted upon creating a vertical type of junction-structure with simple metallic electrodes with the injection of charge carriers into the layers and interface. The low ON–OFF threshold voltage ($\sim$1.25 V) and very high ON/OFF ratio ($\sim 6 \times 10^2$) are promising in energy-efficient 2D MoS_2-based hybrid materials as switching/memory applications. The results are corroborated with the disorder field in 2D MoS_2, which can be controlled by the adjacent antiferromagnetic lattice and directly influences the exchange correlation due to proximity effects.

Disclaimer

Project co-funded by the European Union. However, the views and opinions expressed herein are those of the author(s) only and do not necessarily reflect those of the European Union or European Research Executive Agency. Neither the European Union nor the granting authority can be held responsible for them.

Conflicts of interest

There are no conflicts of interest to declare from the authors.

Data availability

The data for this article, including the experimental datasets with raw data, are available at Mendeley data at **https://doi.org/10.17632/55px8bdhd3.1**. (Bhattacharya, 2025).[99] The dataset contains raw.txt data files for magnetic measurements, zfc fc files, relaxation curves, xrd files for Rietveld analysis, Raman data file, transport data for RT, *J–V* curves, MR data in %, AFM height profile files, *etc.*

Supplementary information (SI) contains Raman analysis, ZFC_FC of pure MoS_2, detail AFM image analysis, XPS measurement protocol, field cooled MH data *etc*. See DOI: **https://doi.org/10.1039/d5ma00565e**.

Acknowledgements

S. B. acknowledges the Japan Society for the Promotion of Science (JSPS) for providing a JSPS International postdoctoral fellowship (standard) (ID P20070) during the initial stages of this work. Researcher S. B. conducted his research under the Marie Skłodowska-Curie Actions–COFUND project, which is co-funded by the European Union (Physics for Future – Grant Agreement No. 101081515) at FZU-Institute of Physics of the Czech Academy of Sciences, Prague, Czech Republic. H. T. and S. B. also thank JSPS for support *via* the Grants-in-Aid for Scientific Research (KAKENHI Project Numbers 22H00315 and 22F20070). I. A. K. acknowledges the support from the Operational Programme Johannes Amos Comenius financed by European Structural and Investment Funds and the Czech Ministry of Education, Youth and Sports (Project No. SENDISO CZ.02.01.01/00/22_008/0004596). T. O. thanks Grants-in-Aid for Scientific Research (KAKENHI Project Number 25H00414) for the research grant.

References

1 K. S. Novoselov, A. Mishchenko, A. Carvalho and A. H. Castro Neto, *Science*, 2016, **353**, 9439.
2 D. Voiry, *et al.*, *Nano Lett.*, 2013, **13**, 6222–6227.
3 J. Kibsgaard, Z. Chen, B. N. Reinecke and T. F. Jaramillo, *Nat. Mater.*, 2012, **11**, 963–969.
4 B. Radisavljevic, A. Radenovic, J. Brivio, V. Giacometti and A. Kis, *Nat. Nanotechnol.*, 2011, **6**, 147–150.
5 B. Radisavljevic, M. B. Whitwick and A. Kis, *ACS Nano*, 2011, **5**, 9934–9938.
6 H. Nam, *ACS Nano*, 2013, **7**, 5870–5881.
7 D. J. Late, *et al.*, *ACS Nano*, 2013, **7**, 4879–4891.
8 A. Castellanos-Gomez, *et al.*, *Nano Lett.*, 2013, **13**, 5361–5366.
9 B. Scharf, G. Xu, A. Matos-Abiague and I. Zutic, *Phys. Rev. Lett.*, 2017, **119**, 127403.
10 X. Liang, L. Deng, F. Huang, T. Tang, C. Wang, Y. Zhu, J. Qin, Y. Zhang, B. Peng and L. Bi, *Nanoscale*, 2017, **9**, 9502.
11 W. Zhang, L. Zhang, P. K. J. Wong, J. Yuan, G. Vinai, P. Torelli, G. van der Laan, Y. P. Feng and A. T. S. Wee, *ACS Nano*, 2019, **13**, 8997.
12 X. Liu, C. Z. Wang, Y. X. Yao, W. C. Lu, M. Hupalo, M. C. Tringides and K. M. Ho, *Phys. Rev. B: Condens. Matter Mater. Phys.*, 2011, **83**, 235411.
13 Y. S. Dedkov and M. Fonin, *New J. Phys.*, 2010, **12**, 125004.
14 T. P. Kaloni, N. Singh and U. Schwingenschlogl, *Phys. Rev. B: Condens. Matter Mater. Phys.*, 2014, **89**, 035409.
15 A. V. Krasheninnikov, P. O. Lehtinen, A. S. Foster, P. Pyykko and R. M. Nieminen, *Phys. Rev. Lett.*, 2009, **102**, 126807.
16 T. P. Kaloni, *J. Phys. Chem. C*, 2014, **118**, 25200.

17 S. P. Tsai and C. Y. Yang, *et al.*, *Adv. Quantum Technol.*, 2021, **4**, 2000104.
18 A. J. Tkalych, K. Yu and E. A. Carter, *J. Phys. Chem. C*, 2015, **119**(43), 24315–24322.
19 A. J. Tkalych, H. L. Zhuang and E. A. Carter, *ACS Catal.*, 2017, **7**(8), 5329–5339.
20 Y. Hao, J. Li, X. Cao, L. Meng, J. Wu, X. Yang, Y. Li, Z. Liu and M. Gong, *ACS Catal.*, 2023, **13**(5), 2916–2927.
21 E. W. Jungner, *Anordning Vid Elektroder for Elektriska Accumulatorer*, *Swedish Pat.*, 8558, 1897.
22 E. W. Jungner, *Electrode for Reversible Galvanic Batteries*, *US Pat.*, 896327, 1908.
23 H. Bode, K. Dehmelt and J. Witte, *Electrochim. Acta*, 1966, **11**, 1079–1087.
24 R. Oesten, M. Wohlfahrt-Mehrens, S. Ströbele, M. Kasper and R. A. Huggins, *Ionics*, 1996, **2**, 293–301.
25 A. Szytula, A. Murasik and M. Balanda, *Phys. Status Solidi B*, 1971, **43**, 125–128.
26 R. Barnard, C. F. Randell and F. L. J. Tye, *Appl. Electrochem.*, 1980, **10**, 109–125.
27 Q. Song, Z. Tang, H. Guo and S. L. I. Chan, *J. Power Sources*, 2002, **112**, 428–434.
28 Y. F. Li and A. Selloni, *J. Phys. Chem. Lett.*, 2014, **5**, 3981–3985.
29 A. J. Tkalych, K. Yu and E. A. Carter, *J. Phys. Chem. C*, 2015, **119**, 24315–24322.
30 H. Jeong, J. Y. Kim, J. W. Kim, J. Hwang, J. E. Kim, J. Lee, T. Yoon, B. Cho, S. Kim, R. Ruoff and S. Choi, *Nano Lett.*, 2010, **10**, 4381.
31 S. Hong, J. Kim, S. Kim, S. Choi and B. Cho, *IEEE Electron Device Lett.*, 2010, **31**, 1005.
32 S. Hong, J. Kim, S. Kim and B. Cho, *J. Appl. Phys.*, 2011, **110**, 044506.
33 L. Wang, W. Yang, Q. Sun, P. Zhou, H. Lu, S. Ding and D. Zhang, *Appl. Phys. Lett.*, 2012, **100**, 063509.
34 T. Jonsson, J. Mattsson, C. Djurberg, F. A. Khan, P. Nordblad and P. Svedlindh, *Phys. Rev. Lett.*, 1995, **75**, 4138.
35 P. Jonsson, M. F. Hansen, P. Svedlindh and P. Nordblad, *Phys. B*, 2000, **284**, 1754.
36 Y. Sun, M. B. Salamon, K. Garnier and R. S. Averback, *Phys. Rev. Lett.*, 2003, **91**, 167206.
37 L. Lutterotti, MAUD™ 2002, version 1 85.
38 H. M. Rietveld, *J. Appl. Crystallogr.*, 1969, **2**, 65.
39 L. Yang, X. Cui and J. Zhang, *et al.*, *Sci. Rep.*, 2014, **4**, 5649.
40 A. Le Bail, Modelling Anisotropic Crystallite Size/Microstrain in Rietveld Analysis, *Appl. Crystallogr.*, 1992, **25**(6), 846–851.
41 R. E. Dinnebier, A. Leineweber and J. S. O. Evans, *Rietveld Refinement: Practical Powder Diffraction Pattern Analysis using TOPAS*, De Gruyter, Berlin, 2019.
42 J. Wei, H. Huang and Q. Luo, *et al.*, *Catal. Lett.*, 2022, **152**, 263–275.
43 T. Nagarajan, M. Khalid, N. Sridewi, P. Jagadish, J. Priyanka, S. Shahabuddin, K. Muthoosamy and R. Walvekar, *Sci. Rep.*, 2022, **12**, 14108.
44 S. Bhattacharya, D. Dinda, B. K. Shaw, S. Dutta and S. K. Saha, *Phys. Rev. B*, 2016, **93**(18), 184403.
45 S. Bhattacharya, W. Choi, A. Ghosh, S. Lee, G. D. Lee and S. K. Kim, *Nanotechnology*, 2021, **32**, 385705.
46 S. Bhattacharya, E. Mathan Kumar, R. Thapa and S. K. Saha, *Appl. Phys. Lett.*, 2017, **110**, 032404.
47 C. A. Schneider, W. S. Rasband and K. W. Eliceiri, *Nat. Methods*, 2012, **9**(7), 671–675.
48 H. Wang, H. Yuan, S. S. Hong, Y. Lib and Y. Cui, *Chem. Soc. Rev.*, 2015, **44**, 2664.
49 K. D. Rasamani, F. Alimohammadi and Y. Sun, *Mater. Today*, 2017, **20**, 2.
50 S. Zhang, Z. Yin and L. Wang, *et al.*, *Energy Mater.*, 2024, **4**, 400065.
51 K. Zhang, P. Li and S. Guo, *et al.*, *J. Mater. Chem. A*, 2018, **6**, 22513–22518.
52 S. Pak, J. Lee, Y. Lee, A. Jang, S. Ahn, K. Y. Ma, Y. Cho, J. Hong, S. Lee, H. Y. Jeong, H. Im, H. S. Shin, S. M. Morris, S. Cha, J. I. Sohn and J. M. Kim, *Nano Lett.*, 2017, **17**(9), 5634–5640.
53 J. U. Lee, S. Woo, J. Park, H. C. Park, Y. W. Son and H. Cheong, *Nat. Commun.*, 2017, **8**, 1370.
54 C. Cai, Z. Tao, Y. Zhu, Y. Tan, A. Wang, H. Zhou and Y. Yang, *Nanoscale Adv.*, 2021, **3**, 3780–3787.
55 P. N. Ghosh and C. R. Maiti, *Phys. Rev. B: Condens. Matter Mater. Phys.*, 1983, **28**, 2237.
56 A. Molina-Sánchez and L. Wirtz, *Phys. Rev. B: Condens. Matter Mater. Phys.*, 2011, **84**, 155413.
57 T. Li and G. Galli, *J. Phys. Chem. C*, 2007, **111**(44), 16192–16196.
58 B. Pacakova, J. Vejpravova, A. Repko, A. Mantlikova and M. Kalbac, *Carbon*, 2015, **95**, 573–579.
59 M. Sadeghi, A. Zelati, S. Rezaee, C. Luna, R. Matos, M. Pires, N. Ferreira, H. Fonseca Filho, A. Ahmadpourian and Ș. Țălu, *Coatings*, 2022, **12**(9), 1364.
60 M. Rajput, S. K. Mallik, S. Chatterjee, A. Shukla, S. Hwang, S. Sahoo, G. V. Pavan Kumar and A. Rahman, *Commun. Mater.*, 2024, **5**, 190.
61 M. Baker, R. Gilmore, C. Lenardi and W. Gissler, *Appl. Surf. Sci.*, 1999, **150**, 255–262.
62 I. S. Kim, V. K. Sangwan, D. Jariwala, J. D. Wood, S. Park, K.-S. Chen, F. Shi, F. Ruiz-Zepeda, A. Ponce, M. Jose-Yacaman, V. P. Dravid, T. J. Marks, M. C. Hersam and L. J. Lauhon, *ACS Nano*, 2014, **8**(10), 10551–10558.
63 A. Curcio, J. Wang, Z. Wang, Z. Zhang, A. Belotti, S. Pepe, M. B. Effat, Z. Shao, J. Lim and F. Ciucci, *Adv. Funct. Mater.*, 2021, **31**, 2008077.
64 D. Ko, X. Jin, K.-D. Seong, B. Yan, H. Chai, J. M. Kim, M. Hwang, J. Choi, W. Zhang and Y. Piao, *Appl. Catal., B*, 2019, **248**, 357.
65 Y. Li, Y. Yu, Y. Huang, R. A. Nielsen, W. A. Goddard, Y. Li and L. Cao, *ACS Catal.*, 2015, **5**, 448.
66 M.-R. Gao, J.-X. Liang, Y.-R. Zheng, Y.-F. Xu, J. Jiang, Q. Gao, J. Li and S.-H. Yu, *Nat. Commun.*, 2015, **6**, 5982.
67 G. M. Wang, Y. C. Ling, X. H. Lu, T. Zhai, F. Qian, Y. X. Tong and Y. Li, *Nanoscale*, 2013, **5**, 4129–4133.

68 S. Narayanaru, H. Kuroki, T. Tamaki, G. M. Anilkumar and T. Yamaguchi, *RSC Sustainability*, 2025, **3**, 1705.
69 N. Weidler, J. Schuch, F. Knaus, P. Stenner, S. Hoch, A. Maljusch, R. Schäfer, B. Kaiser and W. Jaegermann, *J. Phys. Chem. C*, 2017, **121**(12), 6455–6463.
70 C. Mahala, M. Devi Sharma and M. Basu, *ChemElectroChem*, 2019, **6**, 3488.
71 H. Ohldag, A. Scholl, F. Nolting, E. Arenholz, S. Maat, A. T. Young, M. Carey and J. Stohr, *Phys. Rev. Lett.*, 2003, **91**, 017203.
72 I. K. Schuller, R. Morales, X. Batlle, U. Nowak and G. Güntherodt, *J. Magn. Magn. Mater.*, 2016, **416**, 2–9.
73 M. Kiwi, Exchange bias theory, *J. Magn. Magn. Mater.*, 2001, **234**, 584–595.
74 X. Wu, D. Lan, I. Hwang, C. Sun, H. Zhou, X. Yu, P. Yang, X. Yu, C. Liu, P. Chen, J. Ding, J. Chen and G. M. Chow, *J. Alloys Compd.*, 2023, **932**, 167582.
75 M. K. Lee, T. K. Nath, C. B. Eom, M. C. Smoak and F. Tsui, *Appl. Phys. Lett.*, 2000, **77**, 3547–3549.
76 T. L. Meyer, A. Herklotz, V. Lauter, J. W. Freeland, J. Nichols, E. J. Guo, S. Lee, T. Z. Ward, N. Balke, S. V. Kalinin, M. R. Fitzsimmons and H. N. Lee, *Phys. Rev. B*, 2016, **94**, 174432.
77 R. Pentcheva and H. S. Nabi, *Phys. Rev. B: Condens. Matter Mater. Phys.*, 2008, **77**, 172405.
78 M. Bibes, J. E. Villegas and A. Barthelemy, *Adv. Phys.*, 2011, **60**, 5–84.
79 M. Suzuki, I. S. Suzuki and M. Matsuura, *Phys. Rev. B: Condens. Matter Mater. Phys.*, 2006, **73**, 184414.
80 J.-U. Thiele, S. Maat and E. E. Fullerton, *Appl. Phys. Lett.*, 2003, **82**, 2859.
81 N. Khan, P. Mandal and D. Prabhakaran, *Phys. Rev. B: Condens. Matter Mater. Phys.*, 2014, **90**, 024421.
82 Y. Sun, M. B. Salamon, K. Garnier and R. S. Averback, *Phys. Rev. Lett.*, 2003, **91**, 167206.
83 S. Wang, K. Manga, M. Zhao, Q. Bao and K. Loh, *Small*, 2011, **7**, 2372.
84 V. Nagareddy, M. D. Barnes, F. Zipoli, K. T. Lai, A. M. Alexeev, M. Felicia Craciun and C. David Wright, *ACS Nano*, 2017, **11**(3), 3010–3021.
85 X. Zhuang, Y. Chen, G. Liu, P. Li, C. Zhu, E. Kang, K. Noeh, B. Zhang, J. Zhu and Y. Li, *Adv. Mater.*, 2010, **22**, 1731.
86 W. Jie, Z. Yang, F. Zhang, G. Bai, C. Wah Leung and J. Hao, *ACS Nano*, 2017, **11**(7), 6950–6958.
87 K. A. Shaykhutdinov, S. V. Semenov, D. A. Balaev, M. I. Petrov and N. V. Volkov, *Phys. Solid State*, 2009, **51**, 778–780.
88 K. A. Shaykhutdinov, S. I. Popkov, S. V. Semenov, D. A. Balaev, A. A. Dubrovskiy, K. A. Sablina, N. V. Sapronova and N. V. Volkov, *J. Appl. Phys.*, 2011, **109**, 053711.
89 D. Tripathy, A. O. Adeyeye and S. Shannigrahi, *Phys. Rev. B: Condens. Matter Mater. Phys.*, 2007, **76**, 174429.
90 S. Ghosh, P. C. Patel and P. C. Srivastava, *J. Mater. Sci.: Mater. Electron.*, 2017, **28**, 15284–15292.
91 E. DeBiasi, R. D. Zysler, C. A. Ramos, H. Romero and D. Fiorani, *Phys. Rev. B: Condens. Matter Mater. Phys.*, 2005, **71**, 104408.
92 E. De Biasi, C. A. Ramos, R. D. Zysler and H. Romero, *Phys. Rev. B: Condens. Matter Mater. Phys.*, 2002, **65**, 144416.
93 G. Kresse and J. Hafner, *Phys. Rev. B: Condens. Matter Mater. Phys.*, 1993, **47**, 558.
94 P. E. Blöchl, Projector Augmented-Wave Method, *Phys. Rev. B: Condens. Matter Mater. Phys.*, 1994, **50**, 17953–17979.
95 J. P. Perdew, K. Burke and M. Ernzerhof, *Phys. Rev. Lett.*, 1996, **77**, 3865–3868.
96 S. Grimme, J. Antony, S. Ehrlich and H. Krieg, *J. Chem. Phys.*, 2010, **132**, 154104.
97 S. Grimme, S. Ehrlich and L. Goerigk, *J. Comput. Chem.*, 2011, **32**, 1456–1465.
98 A. J. Tkalych, K. Yu and E. A. Carter, *J. Phys. Chem. C*, 2015, **119**(43), 24315–24322.
99 S. Bhattacharya, Evolution of Giant Exchange Bias with Ferromagnetic Ordering and Robust Memory Effect by Strain Engineering MoS_2 in Weak Antiferromagnetic Gating, Mendeley Data, V1, 2025, DOI: 10.17632/55px8bdhd3.1.